AirCargoChallenge 2022

Technical Report

Team #25

Aero@UBI

Acknowledgements

The Aero@UBI team would like to thank the University of Beira Interior (UBI), in particular the Aerospace Sciences Department (DCA) and the Faculty of Engineering (FE) for the support given in the development of this project, since they allowed us to use their facilities for the construction of our aircraft and prototypes. We would also like to thank our sponsors for the financial support that was crucial for the purchase of the appropriate materials for the construction of the aircraft. Finally, our special thanks goes to our Professor in charge, Professor Miguel Ângelo Silvestre, for all his support and guidance throughout the project.

As said before, the team is grateful to all the sponsors:

Diamond Category

- Orion Technik

Gold Category

- AED Cluster Portugal
- Blocks

Silver Category

- AEROUBI & AS Covilhã

- QSR

Bronze Category

- Águas da Covilhã

- Serra Shopping

- 3D Maker

- Danke

Contents

1 Introduction. 1
1.1 Objectives 1
1.2 University da Beira Interior's Participations 1
1.3 Aero@UBI Team 1
2 Project Management. 4
2.1 Schedule 4
2.2 Budget 4
3 Propulsive System 4
3.1 Research 4
3.1.1 Battery Study 4
3.1.2 Propeller 5
3.1.3 Ducted Propeller 8
3.1.4 Motor Controller 9
3.2 Adopted Propulsive System 10
4 Aerodynamic Design 11
4.1 Theoretical Models 11
4.1.1 Finite Wing Aerodynamic Model 11
4.1.2 Airfoil Theoretical Model 12
4.1.3 Take-off Model 12
4.1.4 Structure Mass Model 13
4.2 Small Scale Prototype and Airfoil Selection 13
4.3 Initial Full Scale Prototypes 15
4.3.1 Rhombus Geometry Study 16
4.3.2 Parametric Study 17
4.3.3 Prototypes Preliminary Configuration 17
4.3.4 Airfoil Design 19
4.4 Flap Selection 21
4.5 Final Configuration and Wing Size 21
4.5.1 Stability and Control 21
5 Structural Design 22
5.1 Research 22
5.1.1 Structure Configurations 22
5.1.2 Construction Techniques 24
5.1.3 Construction Test and Materials 24
5.1.4 Structure configuration Mass 25
5.2 Wing 26
5.3 Fuselage 27
5.4 Tail 27
5.5 Tail Booms 27
6 Systems 28
6.1 RX battery & BEC 28
6.2 Receiver and Radio Control 28
6.3 Servos 28
6.4 Data Acquisition System 28
7 Payload Prediction 28

8 Center of Gravity **29**
9 Outlook **30**
10 Drawings **30**
References **30**

1 Introduction

1.1 Objectives

The present report describes the design of the Aero@UBI team's aircraft for the 2022 edition of the Air Cargo Challenge, to be held in Munich, Germany.

With the competition's objectives in mind, our team worked towards the goal of achieving the highest possible score aiming to win the competition, while respecting the restrictions imposed by the regulation.

The aircraft must take off in 60 meters, while carrying the highest possible payload to a height of 100 meters in 60 seconds and achieve the highest possible level flight speed with the most favorable propulsion system configuration allowed by the regulations of the competition. it is assumed that the flight box is wide enough that maneuvering to stay inside is smooth. Thus, not affecting the design of the aircraft.

1.2 University da Beira Interior's Participations

The Aero@UBI team has been participating in Air Cargo Challenge since its first edition in 2003. Having won three of the nine editions of ACC (2003, 2007 and 2011), University of Beira Interior has organized the 2009 and 2013 editions. In the Table 1 all Aero@UBI participations are presented, with their respective classification.

Table 1: History of participation

Edition	Year	Location	Organisation	Classification UBI
1st	2003	Ota, Portugal	APAE	1st place
2nd	2005	Lisbon, Portugal	APAE	3rd and 6th places
3rd	2007	Lisbon, Portugal	APAE & EUROAVIA	1st and 7th places
4th	2009	Covilhã, Portugal	APAE & EUROAVIA	Organising team, 14th place
5th	2011	Stuttgart, Germany	EUROAVIA AS Stuttgart & APAE	1st place
6th	2013	Ota, Portugal	EUROAVIA AS Covilhã	Organizing team
7th	2015	Stuttgart, Germany	EUROAVIA AS Stuttgart	5th place
8th	2017	Zagreb, Croatia	EUROAVIA AS Zagreb	20th and 23rd places
9th	2019	Stuttgart, Germany	EUROAVIA AS Stuttgart	5th place

1.3 Aero@UBI Team

Our team is composed by 7 team members, including the pilot. Since we represent Universidade da Beira Interior, we also have a professor in charge.

Miguel Ângelo Silvestre - Professor in charge

Professor Miguel is one of the longest participating professors at ACC and basically one of the greatest contributors to ACC, organizing 2 and winning 3 of the past editions and participated since the first ACC edition in 2003. He is an Assistant Professor of the Aerospace Sciences Department at UBI and has been the main driver of our University´s efforts at ACC. Miguel is an expert in aircraft performance and propulsion as well as rotary wing aerodynamics. He has been a single piston engine private pilot and is a sailplane pilot and RC modeler since the early 90´s. He holds a PhD from UBI in Aeronautical Engineering and firmly believes in the design, build and operate philosophy.

Pedro Gouveia - Team Leader

Academic Info: Aeronautical Eng., 4th Year **Age:** 21 Years

Since his first year in University he has been involved in projects and competitions. Pedro was Team Leader of *Cheroavias*, a portuguese team of 5 members which won the first edition of the Airbus Sloshing Rocket competition. During his 2nd year, he was invited to present his work at the 5th Sloshing Symposium, to professionals from ArianeGroup, Airbus and ESA. More recently, he was invited to join the propulsive subsystem of the first amateur rocket team from UBI, Fénix Rocket Team, where he is one of the founding members. He was responsible for the parametric studies of the aircraft.

Guilherme Pangas - Team Member

Academic Info: Aeronautical Eng., 4th Year **Age:** 21 Years

Guilherme is passionate about the developing of UAVs. He is now trying to develop is own 3D printer with the purpose that in a close future be capable of print of is own aircraft. In this team, he worked in the structural design and simulation and help in the constructive tests.

Hugo Sousa - Team Member

Academic Info: Aeronautical Eng., 4th Year **Age:** 21 Years

Hugo is always seeking to learn new things, is passionate about UAVs and formula one but also finds space fascinating. He has been involved in the design of a Solar Autonomous Research Aircraft, with the goal to be an affordable aircraft for persistent wildlife monitoring. This project was a collaboration between University of Beira Interior and Faculty of Engineering of U.Porto and he was responsible for the the design of the tail, the ribs of the wing and assembly and manufacturing processes. In his free time, Hugo is developing an aircraft to learn how to pilot and a racing drone. For this competition, he was responsible for the optimization of the airfoil and worked on the CAD of the aircraft.

Joana Santos Silva - Team Member

Academic Info: Aeronautical Eng., 5th Year **Age:** 22 Years

During her 3rd and 4th years, Joana took part of the *Rocket Buddies* team. This team was created by 5 Aeronautical Engineering students from UBI, with the aim of participate in the 2nd edition of Airbus Sloshing Rocket Workshop competition, which they have won. She was invited to participate in the 6th Airbus/Ariane Sloshing & Ditching Symposium to present the work developed. Joana is currently working on her Master's Thesis on experimental analysis on a plunging NACA 0012 airfoil motion with unequal ascending and descending velocities. She was responsible for the propulsive system and worked in the constructive tests.

Luís Ferreira - Team Member

Academic Info: Aeronautical Eng., 5th Year **Age:** 22 Years

Luís was part of the *Rocket Buddies* team, participating and winning the second edition of the Airbus Sloshing Rocket Workshop. Participated in the 6th Airbus/Ariane Sloshing & Ditching Symposium to talk about the work developed. He is also the coordinator of the structures team of the Fénix Rocket Team, the first amateur rocket team from UBI. Currently, he is working in his Master's Thesis on Multidisciplinary Design Optimization of Air Cargo Challenge aircrafts. In this team, he worked in the constructive tests and on the CAD.

Pedro Belizário - Team Member

Academic Info: Aeronautical Eng., 5th Year **Age:** 22 Years

Pedro is a student in his final year of the Integrated Master's Degree in Aeronautical Engineering. He likes airplanes, robots and machine learning. Hence, he is pursuing his Master's Thesis on nonlinear control using neural networks.

António Vilaça - Pilot

Academic Info: Aeronautical Eng., 3rd Year **Age:** 20 Years

António has been modelling airplanes since he was 5 years old. When he was 9 years he won the national airplane piloting championship in F3P indoor cathegory (Precision Acrobatics). He has been a demonstration pilot at national and international model aircraft festivals, and worked as a test pilot for a Rc aircraft factory specialized in aluminum model airplanes. António has taken part in the Aero@UBI Team in order to compete for the Shell Eco-Marathon 2020. More recently, he has been invited by the Portuguese Air Force to lesson some of the military about drone piloting, and participated in multiple operations with unmanned aircraft vehicles from the Portugues Air Force

2 Project Management

2.1 Schedule

The project management aims to establish a calendar that includes the deadlines defined by the regulations as well as the dates established by the team for each task. Since it is the first time all team members participate in the Air Cargo Challenge, an organised schedule and a review of the work done by previous teams is important to understand which type of limitations and challenges we might encounter during the project development. As such, for the preparation of the Air Cargo Challenge 2022, our team held weekly meetings to discuss about the aircraft and to help each other with each task. Table 2 presents the schedule defined by our team for the ACC2022. The brown color refers to a period of heavy Covid-19 restrictions in our country.

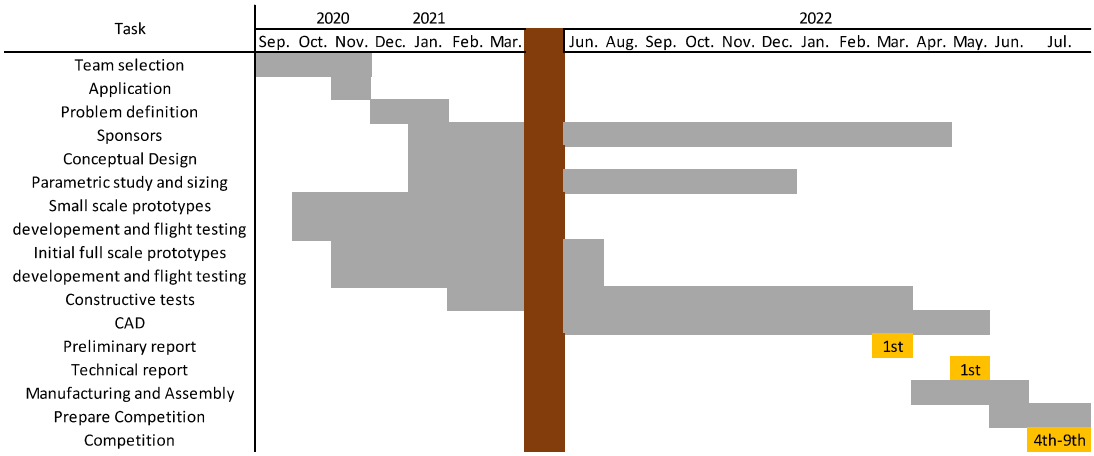

Table 2: Project Schedule

2.2 Budget

The project's budget is usually a limitation when selecting the materials and manufacturing processes to be used in the aircraft construction. Our budget of 1500€ is allocated to materials, tools and components that are being used for the aircraft development. Table 3 shows our budget for this year's edition. The over budget will be used for unpredicted incidents that might happen during the manufacture of the final aircraft.

3 Propulsive System

3.1 Research

3.1.1 Battery Study

Batteries research is very important because they can largely influence the performance of the propulsion system. So, the objective of this work was to identify the best battery, i.e., with the least mass and just enough capacity for the flight (full power for 180 seconds), but with the highest possible mean voltage during the take-off and climb phase (initial 80 seconds). A set of candidate batteries were purchased and to test the batteries, an experimental setup was implemented. The equipment to test the batteries included:

Item	Cost (€)
Propeller (x4)	60
Motor (x2)	240
Servos (x12)	40
Motor battery (x2)	110
RX battery	12
Plaster & burlap for molds	50
PLA (3D Printer)	80
Extension cables	10
EPS	6
Glass and Carbon fiber	250
Two component polyurethane foam	40
Fuel spent on trips	45
Total	943

Table 3: Materials and components budget

two Arduino Nano, one MOSFET, three sensors (temperature, voltage and current), a power supply and one 3D printed box made from ABS to withstand the temperature. Additionaly, the airplane motor, ESC and R/C system were used to draw the batteries current in realistic conditions. The test consisted in doing various discharges with the motor at full throttle (simulating the throttle that will be used in competition). During each test, the time, voltage and current were recorded. The procedure was repeated with heated batteries (50 °C) and cooled ones.

The results of our research, in figure 1, show that significant voltage differences occur in the final of the flight (200s). The higher the voltage, the higher will be the speed and current of the motor, thus, the propulsive power is roughly proportional to the voltage squared. Heated batteries were identified as having higher voltage under load and did not seem to require significant cooling for the 200 seconds flight duration (at least those of high rated discharge specification that were tested). Thus, heated batteries have more performance in the initial take-off and climb. Data from heated batteries tests are presented in Figure 1. Battery Turnigy Bolt 2400mAh although in the graph it does not hold up to 200s because for cruising flight the current is 19 A, i.e., lower than what is tested here. Battery Ultimate 6400 mAh 3S seems to have a better performance, but has much more capacity and weight than the others, so it is far from the final stage of his discharge in a flight of 200 seconds.

Fig 2 shows the energy vs the mass of the tested batteries that could complete the task. The Turnigy Bolt 2400 mAh (High Voltage, 4.35 V/cell specification) (Figure 3), having just enough energy for the flight task and the least mass is the chosen battery for our aircraft.

3.1.2 Propeller

According to Air Cargo Challenge 2022 Regulations, the aircraft is allowed to use one propeller on the aircraft and the teams may choose between:

- APC-E 10x6E
- Aeronaut CAMcarbon Light 10”x6”

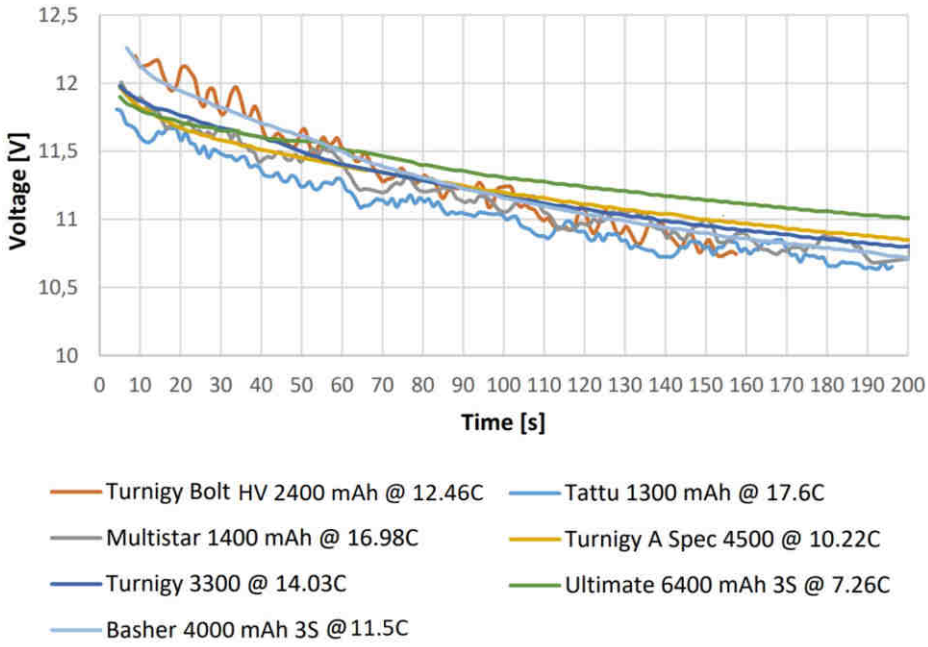

Figure 1: Heated batteries performance data

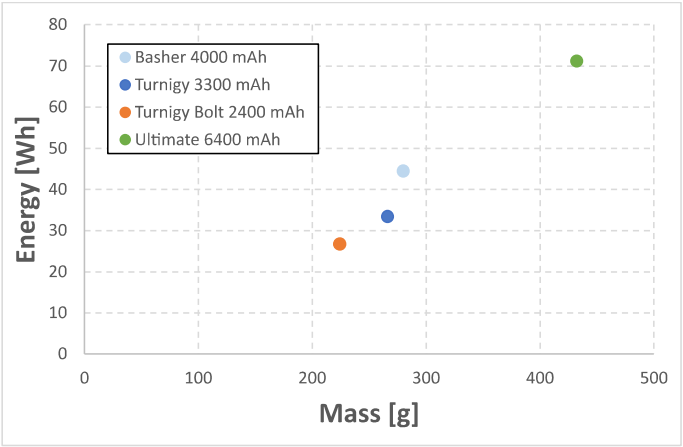

Figure 2: Comparison of the specific energy of all batteries

With these two options for the propeller, it was necessary to define the one that better suits our needs. Through the work conducted by Viktor [5], the two propellers were compared in wind tunnel tests realized at an altitude of 550 m using the Electronic Speed Controller (ESC) Phoenix ICE 75 ESC at 12kHz PWM rate for a constant full throttle 12V motor voltage. The following graphs were obtained for each propeller:

- Thrust generated and current drawn at full throttle, for different freestream velocities (Figure 4);
- Thrust coefficient, C_T, and power coefficient, C_P, as functions of advance ratio, J (Figure 5);
- Propeller efficiency, η_p, as a function of advance ratio, J (Figure 6);
- Thrust/Current, as a function of airspeed at full power (Figure 7).

Figure 3: Chosen Battery

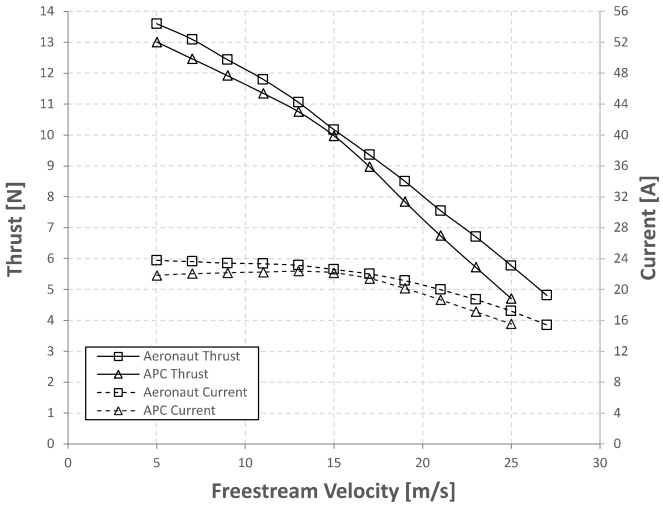

Figure 4: Full throttle thrust and current versus airspeed for both propellers [5]

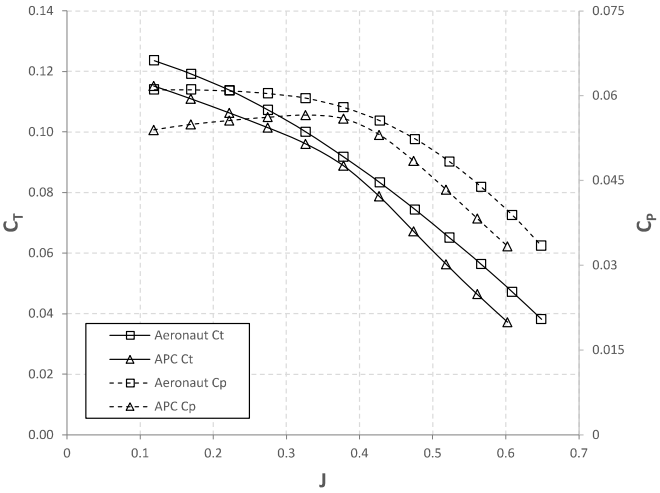

Figure 5: Full throttle thrust coefficient and power coefficient versus advance ratio for both propellers [5]

Through the observation of Figures 4, 5 and 6, it is possible to compare the two propellers under study and draw some conclusions. In Figure 4 we notice that at any freestream velocity, the Aeronaut propeller generates more thrust than the APC, and also consumes more current. Figure 7 shows the ratio Thrust/Current corresponding to the results of Figure 4. So, we see that the propulsive system with the APC propeller appears to be slightly more efficient at lower freestream velocities, being surpassed by the Aeronaut propeller at about 16m/s m roughly the highest propulsive power airspeed of the system. Thus, we can conclude that the best propeller option is the Aeronaut 10”x6”, due to the fact that even generating higher thrust at every airspeed, is more efficient at wind speeds above 16m/s, where the aircraft will spend most of the flight time. So, despite offering a higher propulsive power and energy for the flight, consumes a smaller energy from the battery, allowing the use of a lighter battery.

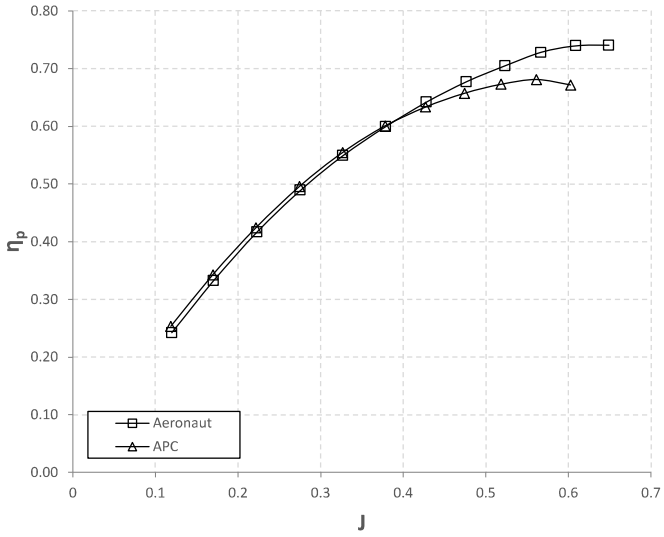

Figure 6: Full throttle propeller thrust versus airspeed for both propellers [5]

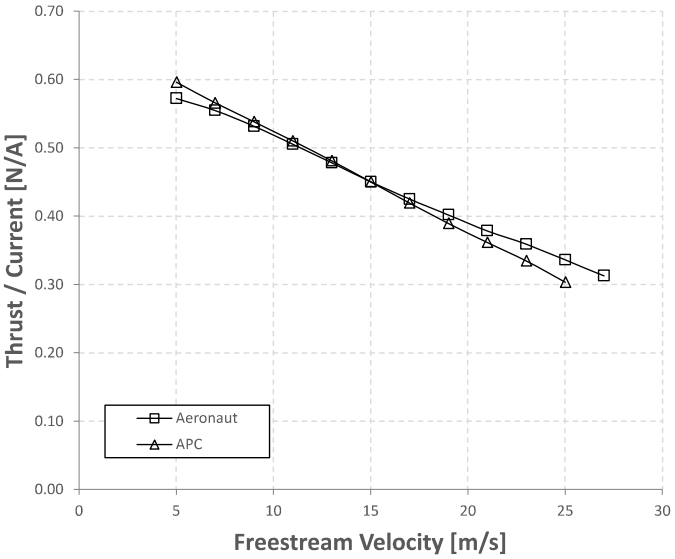

Figure 7: Propulsion efficiency versus airspeed for both propellers [5]

3.1.3 Ducted Propeller

The use of a duct around the propeller can translate into an advantage in terms of maximum thrust available for the same motor and propeller. This configuration consists of using a ring with an aerofoil section around the propeller. A duct was designed using *Ducted Fan Design Code* (DFDC), and then manufactured using 3D FDM printing technology for validation tests in the wind tunnel by Edson [3]. Figure 8 shows a picture of the tested ducted propeller (the APC was thought to be better suited because of its blade tip shape).

Figure 8: Ducted Propeller [3]

With the wind tunnel studies it was determined that the DFDC numerical results were optimistic and the actual performance of the propulsive system with the ducted propeller was lower than the free propeller for airspeed higher than 10m/s. With these results, despite allowing a shorter take-off or a higher mass to

take-off in 60m, the ducted propeller is not recommended to be used, since the aircraft will spend most of the time above 10m/s (roughly the aircraft's stall speed).

3.1.4 Motor Controller

With traditional ESCs, for a given voltage supply, there is a maximum rotational speed for a given brushless permanent magnets motor, known as base speed. This limit is reached when the speed is such that the back electromotive force voltage (U_{bemf}) is the same as the supplied voltage, and the inverter can no longer push current into the stator coils. Field Weakening is a modern technique that allows the increase of the speed of an electric motor. Forcing negative current to the d axis of the motor will cause the rotor magnetic flux to be reduced and will, therefore, decrease the U_{bemf}, allowing the base speed to be exceeded. Making possible to achieve much higher torque, just below the increased motor base speed. On the other hand, torque is proportional to field flux, so, while the rotational speed is increased, the torque per unit Amp is reduced. This means that more current is required to reach the same motor torque, reducing the motor efficiency. In Figure 9 it is possible to observe the Field Weakening region, as well as the maximum torque, maximum power and maximum rotor flux. Only the shape of the plots should be considered.

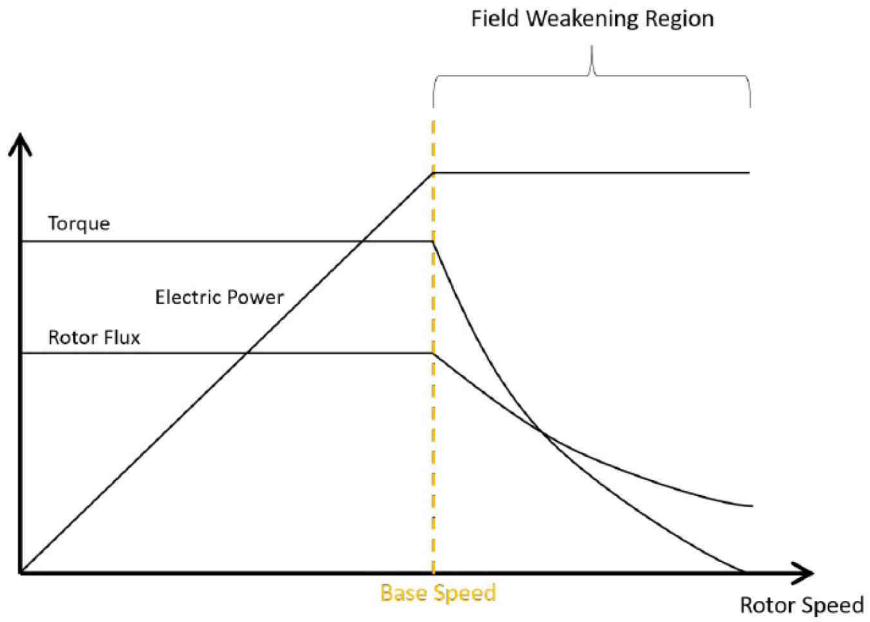

Figure 9: Field Weakenign Region [5]

Viktor [5] tested different field weakening magnitudes in wind tunnel, using a Triforce A50S ESC and the chosen Aeronaut propeller. The Triforce A50S ESC was used because it is commercially available and runs the VESC software that supports field-oriented control and field weakening.

As shown in Figure 10, the effect of field weakening is significant at any airspeed. At 5m/s, the thrust difference between no field weakening and $L_d - L_q$ of 4µH is about 1.2N (a roughly 8% increase) while increasing the drawn current significantly.

Figure 11 shows the Thrust/Current ratio, corresponding to Figure 10 values. It is possible to observe that the setup is less efficient ate generating thrust for lower airspeed, having a noticeable difference. As the freestream velocity increases, this difference becomes less noticeable, meaning that despite the fact that the motor's efficiency drops with more intense field weakening, the global propulsive system efficiency

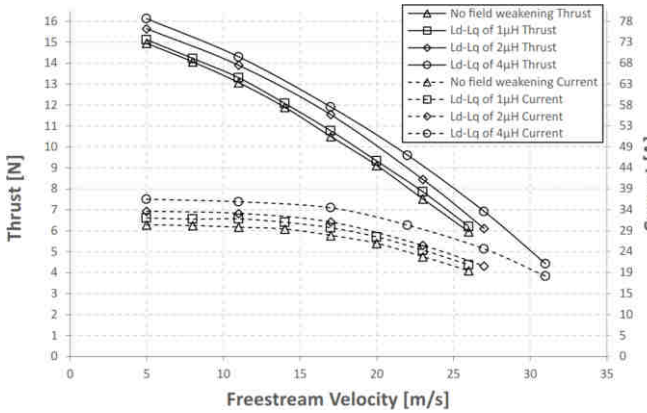

Figure 10: Full throttle thrust and current versus airspeed for different magnitudes of field weakening [5]

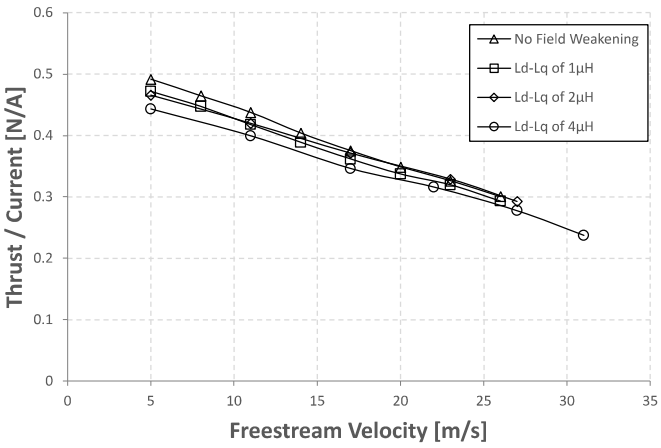

Figure 11: Full throttle Thrust/Current versus airspeed for the different magnitudes of field weakening [5]

is practically unchanged. So, as for the Air Cargo Challenge 2022 aircraft, since our expected cruise speed is higher than 25m/s, it is possible to use field weakening because it will not have a noticeable drop in global propulsive system efficiency at high cruise airspeeds. Therefore, it will not affect significantly, the necessary battery capacity and mass.

Figure 12 shows the RPM values for the same conditions, proving that the field weakening is working and the motor is able to spin faster as the value of $L_d - L_q$ increases.

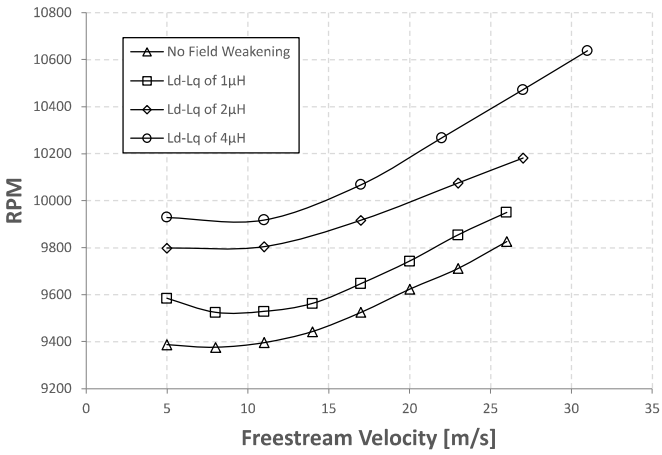

Figure 12: Full throttle RPM versus airspeed for the different magnitudes of field weakening [5]

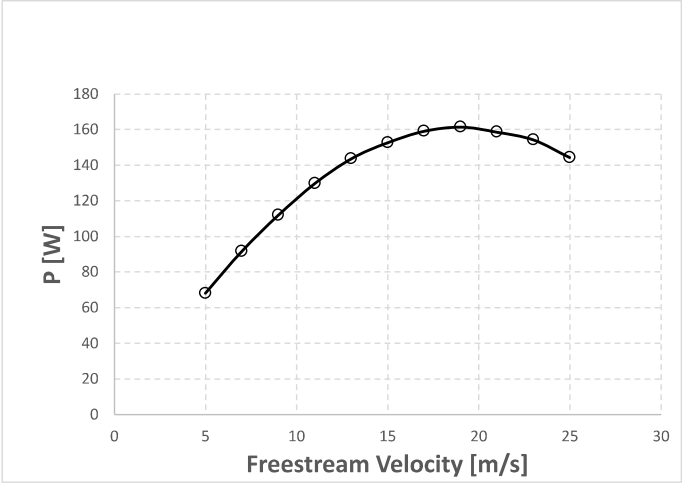

Figure 13: Power versus airspeed

Through Figure 13 it is possible to see that the maximum power occurs for airspeed of approximately 19m/s. This means that we will maximize C_L/C_D for the lift coefficient of 0.8 (lift coefficient correspondent to this airspeed value).

3.2 Adopted Propulsive System

According to the regulations an unmodified AXI 2826/10 GOLD LINE V2 as per rule 4.4.5. As explained in section 3.1.2, the propeller Aeronaut CAMcarbon Light 10”x6” was adopted. The connection between

motor and propeller is made using the stock motor propeller adapter. This ensures that the rotation ratio is one to one, as mandatory. Triforce A50S ESC allows the use of field weakening but proved to be working close to its thermal limit. Therefore, its adoption will depend on the final flight testing of the aircraft. So, the Phoenix ICE 75 ESC at 12 kHz PWM Rate was selected as providing the design final propulsive system performance.

Equation 1 is a second degree polynomial approximation of the thrust as a function of airspeed measured in the wind tunnel for the chosen propeller and without field weakening [5]. In our aircraft design calculations, the considered thrust was further corrected by a factor of the square of the ratio battery voltage by the 12V used throughout the tests. A correction for the air density was also considered for calculation of the payload versus altitude performance. The thrust was considered proportional to the ratio of air density to 550m altitude air density (the altitude where the wind tunnel tests were performed).

$$T = -4.74078 \cdot 10^{-3} V^2 - 2.54289 \cdot 10^{-1} V + 1.50772 \cdot 10^{1} \tag{1}$$

4 Aerodynamic Design

The aircraft's aerodynamics is a key factor for this competition. Four objectives need to be optimized to have the best design: maximize lift-to-drag ratio (L/D) near 17m/s best climb airspeed(maximum propulsive power airspeed); maximize C_L for take-off while maintaining an acceptable L/D for initial acceleration after lifting off; minimize the parasitic drag. In the present section, all the steps that led to the final aerodynamic characteristics of the final aircraft are presented by chronological order.

4.1 Theoretical Models

4.1.1 Finite Wing Aerodynamic Model

The wings aspect ratio is $A = b/c$, where c, where b is the wings span and c is the mean wing chord (for simplification, the aerodynamic mean chord was considered to be equal to the geometric wing chord). Equation (2) is used to calculate the wing lift coefficient by applying a correction factor to the airfoil lift coefficient (C_l).

$$C_L = \frac{C_l}{1 + \frac{C_l}{\pi e A}} \tag{2}$$

where e is the Oswald's efficiency factor which is considered as 0.95 corresponding to the Prandtl lift distribution [2].

The finite wing induced drag, C_{Di}, is modelled by Equation (3).

$$C_{Di} = \frac{C_L^2}{\pi e A} \tag{3}$$

The wing lift, L, is calculated according to Equation (4) and equals the aircraft weight in level flight and small climb angles, $W = mg$.

$$L = W = \frac{1}{2} \rho V_\infty^2 C_L S \tag{4}$$

where ρ is the ISA (International Standard Atmosphere) air density, that is a function of the altitude. A value of 1.165 kg/m^3 was considered for Munich altitude of 520mm, V_∞ is the freestream airspeed, $S = bc$ is the wing reference area.

To calculate the drag, D, the aircraft drag coefficient, C_D, is used according to Equation (5).

$$D = \frac{1}{2}\rho V_\infty^2 C_D S \tag{5}$$

The aircraft's drag coefficient is:

$$C_D = C_d + C_{D_i} + C_{D_{tail}} + C_{D_{misc}} \tag{6}$$

where, C_d is the airspeed drag coefficient, determined dividing C_l by C_l/C_d calculated from equation (8), $C_{D_{tail}}$ is the stabilizers drag coefficient, that was initially assumed to be 30% of the wing's airfoil drag coefficient, $C_{D_{air}}$. C_{D_misc} is a drag relative to all the items not considered separately. E.g, antennas, landing gear wheels and skids, tail booms, air inlets and outlets, wing-fuselage interference drag, etc...

$$C_{D_{fus}} = \frac{k \cdot S_{x_{fus}} \cdot C_{D_{x_{fus}}}}{S_{wing}} \tag{7}$$

coefficient, where k is an arbitrary correction factor for the fuselage drag merit, $S_{x_{fus}}$ is the fuselage frontal area, $C_{D_{x_{fus}}}$ is the fuselage drag coefficient base on the frontal area.
where $C_{D_{misc}}$ is a drag relative to all the items not considered separately. E.g, antennas, landing gear wheels and skids, tail booms, air inlets and outlets, wing-fuselage interference drag, etc.

4.1.2 Airfoil Theoretical Model

To investigate the effect of the airfoil lift coefficient and calculate the airfoil drag coefficient, since at this stage, the airfoil is not defined yet, a generic model that mimics the maximum C_l/C_d as a function of C_l and Reynolds number is used: Re to be expected from a properly designed airfoil. Equation (8) describes this model.

$$\frac{C_l}{C_d} = 58 \sin\left(1.4 C_l^{0.7}\right) \left(\frac{\log\left(Re\sqrt{Cl}\right)}{\log(100000)}\right)^{5.5} \tag{8}$$

using the air viscosity, $\mu = 1.77294 \cdot 10^{-5}$ kg/(ms) and the Reynolds number:

$$Re = \frac{\rho V_\infty c}{\mu} \tag{9}$$

4.1.3 Take-off Model

The lift-off velocity, V_{LO}, can be determined as follows:

$$V_{LO} = 1.2 \cdot V_S - V_{wind} \tag{10}$$

where V_S is the stall velocity, that can be calculated by Equation (11)

$$V_S = \sqrt{\frac{2W}{\rho A C_{L_{max}}}} \tag{11}$$

and the wind speed, V_{wind} is considered to be 1.5 m/s. An optimistic initial value of 1.9 was used for $C_{L_{max}}$, but was later changed, when an actual airfoil was adopted, to a more realistic value of 1.6 (see subsection 4.3.4.

The take-off distance, x_{TO}, can be determined by Equation (12).

$$x_{TO} = \frac{W \cdot V_{LO}^2}{2g\left[T - D - \mu(W - L)\right]_{0.85V_{LO}}} \tag{12}$$

where μ is the friction coefficient, that is considered to be equal to 0.05 for a lawn runway. The thrust force, T, was calculated using the polinomial regression presented in equation (1).

4.1.4 Structure Mass Model

The Aircraft mass is modelled as a function of wingspan and chord, by Equation (13)

$$m = W_{0_{ref}} \left(\frac{b}{b_{ref}}\right)^{e_b} \left(\frac{c}{c_{ref}}\right)^{e_c} + W_{sys} \tag{13}$$

where $W_{0_{ref}}$ is a reference airplane model weight with the same structure concept (including material and building technology), b_{ref} and c_{ref} are the respective reference wingspan and mean chord. In the present case, $W_{0_{ref}} = 0.5$kg, $b_{ref} = 1.4$m and $c_{ref} = 0.2$m were used; e_b and e_c are exponents that reflect the non-linearity of the empty weight function with the airplane wingspan and chord. The values $e_b = 0.75$ and $e_c = 1.5$ were adopted; W_{sys} is the systems weight. In this case, to account for motor, ESC, Rx, battery, propeller, servos and wiring, a $W_{sys} = 0.7$kg.

The aircraft mass model constants $W_{0_{ref}}$, e_b, e_c, b_{ref} and c_{ref} are determined through structural construction experiments and known previous aircraft's empirical data.

4.2 Small Scale Prototype and Airfoil Selection

The first approach would be to find out which of the initial airfoil geometries would be the most efficient for our aircraft, either low, medium or high cambered and either thin or thick. Three distinct airfoils were tested, as shown in Figure 14. With these airfoils, three different wings were manufactured, with the same wingspan but not the same mean chord, c_{mean}. The airfoils' maximum camber and thickness, and respective locations along the chord are displayed in Table 4.

The Selig airfoils are widely known for their high performance at relatively low Reynolds number. The *NewFoilACC2017D* and *MARS_ACC2017_Best* were designed for the Air Cargo Challenge 2017 competition. Initially, only these later two airfoils were considered. It was only after that the team pondered the possibility of testing a thinner airfoil, with a greater mean chord for a lower cruise lift coefficient that the Selig's S9000 airfoil was added to this experimental study. The different wings were tested with the same fuselage and tail such that $c_{mean} \cdot C_{L_{cruise}} = const$, resulting in the same wing lift for all three sets of wings.

	Thickness [%]	at [%]	Camber [%]	at [%]
S9000	9.01	28.73	2.37	41.94
MARS_ACC2017_Best	10.03	26.23	3.75	39.64
NewFoilACC2017D	11.44	25.26	5.09	50.14

Table 4: Preliminary airfoils maximum camber and thickness, and according positions.

For the tested three wing sets, Table 5 presents the three different aircrafts' geometric characteristics, as well as the design $Re\sqrt{C_L}$ for each one of them. In the tests conducted, high and low speed laps were timed with each lap covering a straight line of 106 meters. Time measurements were always performed in

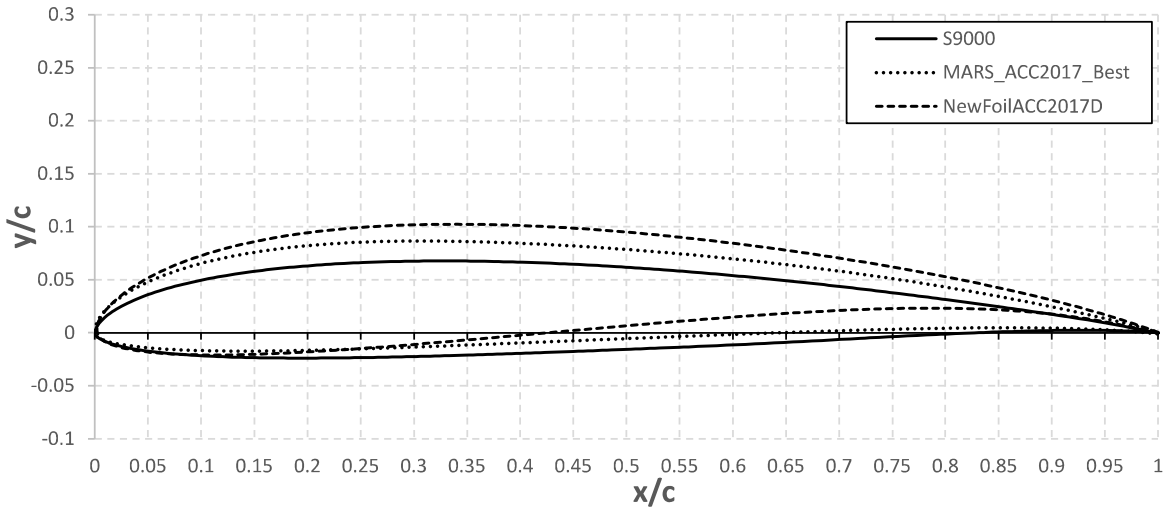

Figure 14: Preliminary airfoil alternatives for the small scale prototype.

	b [m]	c_{mean} [m]	W_{empty} [kg]	$W_{payload}$ [kg]	W_{TO} [kg]	$Re\sqrt{C_L}$
S9000	1.20	0.165	0.828	0.112	0.940	96 045
MARS_ACC2017_Best	1.20	0.138	0.710	0.180	0.890	77 724
NewFoilACC2017D	1.20	0.134	0.795	0.080	0.875	75 104

Table 5: Aircraft geometric characteristics, and flight condition details.

low wind atmospheric conditions upon the return of the aircraft to the initial position, in order to balance the still possible wind effects.

To analyse and decide which one would be the most suitable wing for the aircraft, two different graphs were used, those of Figure 15 and Figure 16. In both of these graphs, the two wings built with the less cambered airfoils (S9000 and MARS_ACC2017_Best) were also tested with a full span flaperon configuration to maximize the lift coefficient. The NewFoilACC2017D did not get to use flaperons due to its realized much lower high speed cruise performance. In Figure 15, lift-to-drag ratio versus lift coefficient of the three aircraft, including with with the flaperon configuration is shown. In Figure 16, cruise drag versus airspeed for each of the aircraft and flaperon configuration for the two wings previously discussed is displayed. The propulsive system curve presented (T) is a linear regression from the actual propulsive system thrust curve, obtained by simulating the propeller with PropSelector software and the battery motor set by simple DC motor theoretical model. It is not the same as Equation 1.

Although there are some minor discrepancies in the results (minimum velocity of the high cambered airfoil - NewFoilACC2017D - without flaperons being higher than the minimum velocity of the low cambered airfoil - S9000), probably due to being the most affected by the lower Reynolds number (75 104), it is notable the higher performance (L/D) the aircraft utilizing the S9000 airfoil at high airspeed ($C_L \approx 0.24$) when compared to the other 2 aircraft. Furthermore, it is also perceptible that despite the S9000 not being the airfoil with the highest $C_{L_{max}}$, when flaperons are implemented, it improves its maximum lift coefficient, to a greater extent than with higher cambered airfoils. On the other hand, the usage of a negative deflection on the flaperons of the NewFoilACC2017 improves its lift-to-drag ratio at low lift coefficients greater than it does on the S9000. Since the S9000 is already an airfoil designed for higher speeds, it will not make the best use of negative flaperon deflections. With these results the team concluded that a low

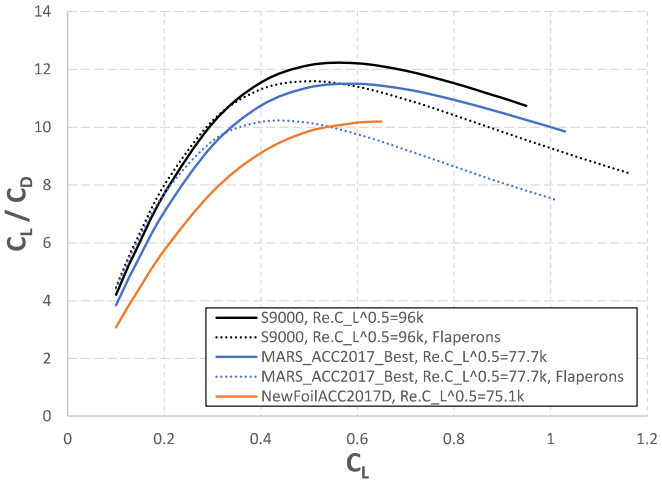

Figure 15: Lift-to-drag ratio, C_L/C_D, versus lift coefficient, C_L, for each aircraft configuration tested.

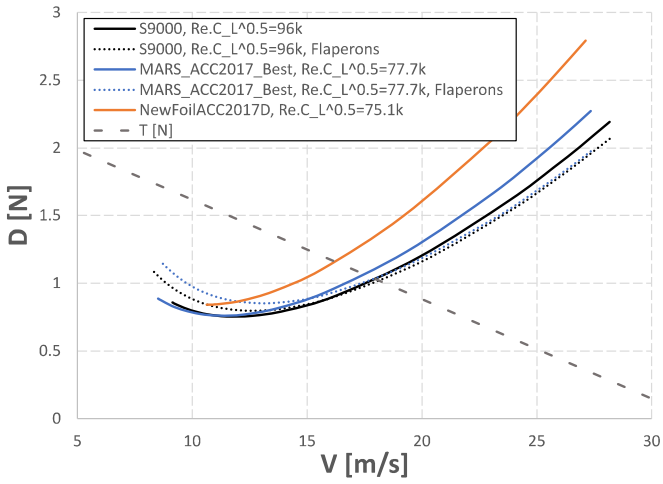

Figure 16: Total aircraft drag, D, versus total velocity, V, curves, for each aircraft configuration tested.

cambered airfoil would be the best choice for the present edition of Air Cargo Challenge.

The performance of these small scale prototypes was initially predicted with XFLR5 before this experimental study. It is important to mention that the experimental curves were obtained by fitting a parabolic drag polar to the obtained experimental points.

Due to the lower Reynolds number and lower expected flaperon improvement (since this airfoil is already the most cambered), the NewFoilACC2017D was discarted without actually testing the flaperon effect.

In order to validate the XFLR5 theoretical method implemented, both experimental and theoretical drag versus velocity (Figure 17) and lift-to-drag ratio versus lift coefficient (Figure 18) curves of the S9000 small scale prototype were compared. It is easily noticeable the difference at higher C_L values. This is probably due to experimental value corresponding to the actual minimum cruise airspeed that was measured, not the actual airplane stall speed. On the other hand, it is possible to see an improvement of the experimental results at higher airspeed, when compared with the theoretical ones. This happens because a drag area was added in the XFLR5 analysis, probably greater than it needed to be. However, this allowed us to rectify that additional drag area value and correct it in the later analyses of the full scale prototypes.

4.3 Initial Full Scale Prototypes

After deciding the base airfoil for the aircraft, it was time to design an actual wing capable of optimizing the objectives of the competition. With the design of the wing, it was also possible to predict a take-off weight for the aircraft. In order to do this, the following objectives needed to be optimized:

- **Climb:** The aircraft has 60s to climb up to 100m. Furthermore, it is evident that maximum payload will be achieved if the full 60s are utilized. What this means is that the wing would need to be designed for a climb rate of 1.667m/s. If we consider that the take-off acceleration takes about 7s, the design climb rate must be about 1.89m/s.

- **Take-off:** The aircraft needs to take-off either in 60m, or in 40m for bonus points. It was initially decided that if wings are designed for 40m take-off, the wings area gets too high and the aspect ratio too low, so the climb will be less effective, limiting the take-off mass and payload to a worse

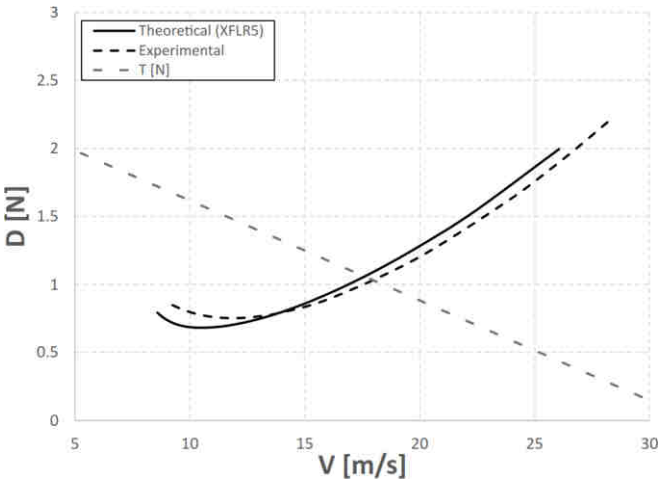

Figure 17: Theoretical and experimental cruise aircraft drag, D, versus airspeed, V, for the S9000 airfoil.

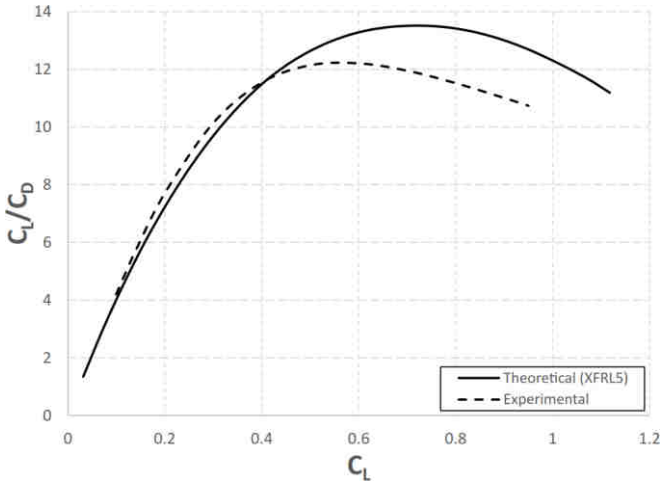

Figure 18: Theoretical and experimental lift-to-drag ratio, C_L/C_D, versus lift coefficient, C_L, curves for the S9000 airfoil.

classification loss than the bonus that would be gained in a 40m take-off. So, the wings were designed so that the aircraft takes off in 60m.

4.3.1 Rhombus Geometry Study

The assembled "flight ready" aircraft needs to fit inside a rhombus (presented in Figure 19), with a maximum height if 0.5m. The length of each side, l, is 1.5m. In order to analyse how the maximum tail-to-nose, l_0, and maximum span, b_0 distances change with the rhombus semi-angle, α, a study has been performed. The results are displayed in Figure 20.

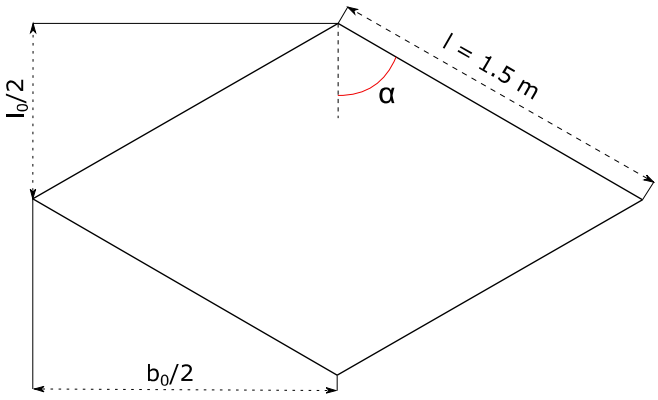

Figure 19: Rhombus geometry established by the ACC 2022 regulations.

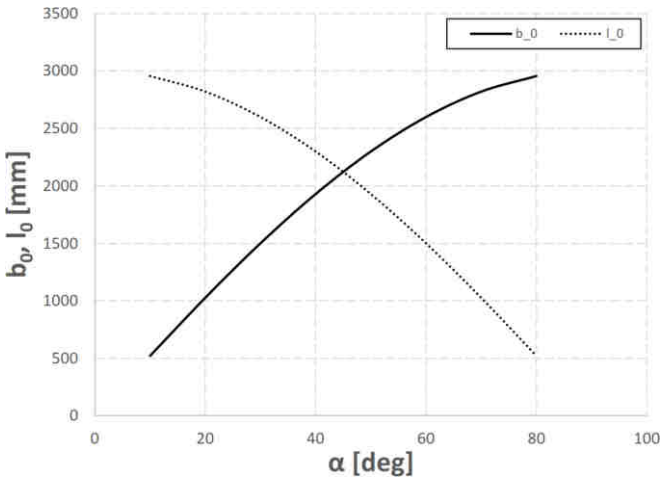

Figure 20: Tail-to-nose, l_0 and wingtip distance, b_0, as a function of the rhombus nose semi-angle, α.

One can see an almost linear decrease of the l_0 length for $\alpha > 45°$. The opposite happens for the maximum span, b_0 distance, as it greatly decreases for $\alpha < 45°$. As an initial approach, in order to maximize the span for the design of the main initial full scale prototype (See subsection4.3), $\alpha = 66°$, which, greatly limited

the tail arm $l_H \approx \frac{l_0}{2}$. With l_0 of about 1500mm, having the value in the middle of the linear region of the curve presented in Figure 20. The flight tests of the main initial full scale prototype proved that the vertical tail was not very effective and to correct the issue, the initial V tail was changed for a T tail, to improve the directional stability. So, the rhombus semi-angle was further studied, and it was concluded that the more appropriated for our final aircraft would be α close to $60°$. A greater angle would unnecessarily reduce the tail arm.

4.3.2 Parametric Study

The equations presented in the subsection 4.1, were implemented in a spreadsheet, in order to find the most suitable mean chord, c_{mean}, and wings span, b. After the small scale prototype tests, a miscellaneous drag coefficient, $C_{D_{misc}} = 0.0161$ was adopted as a good approximation to make the XFLR5 simulations be representative of the actual performance. In Figures 21 and 22, the results that led to the adopted mean chord and span are presented. It can be seen that an increase of b from x to y (4%) reduces the optimal c_{mean} by about 1.74%, corresponding to an increase in W_{TO} of about 1%.

The final c_{mean} utilized was 0.185cm, and the wingspan b was 2.56m, corresponding to a rhombus semi-angle $\alpha = 58.6°$. The takeoff distance for this configuration with no wind is 67m. However, this is considered unrealistic, since there is, in general, some head wind. So, a head wind speed of 1.5m/s is considered for the design to take-off in 60m. The total take-off weight achieved is 52.62N at sea level, and 50.15 N at 520m altitude (Munich).

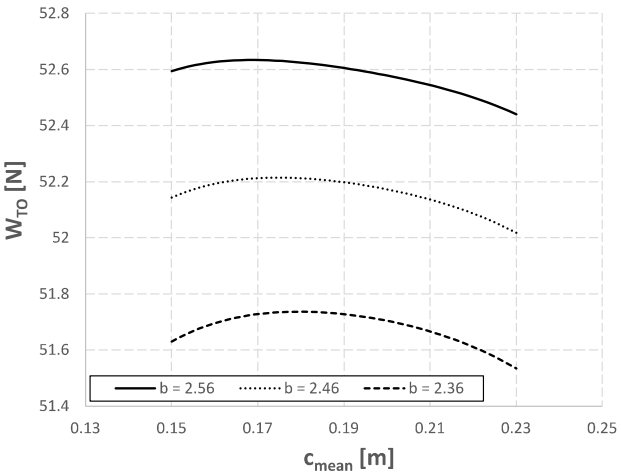

Figure 21: Take-off weight, W_{TO} versus mean chord, c_{mean}, for different wingspans, b, for a climb rate of 1.89m/s, at sea level.

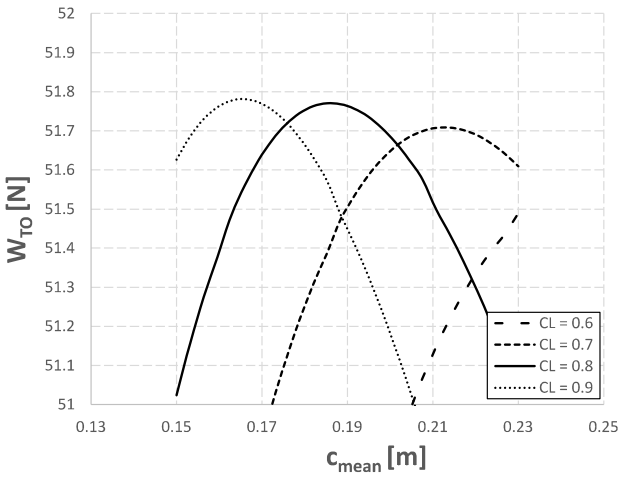

Figure 22: Take-off weight, W_{TO} versus mean chord, c_{mean}, for different lift coefficients, C_L, for a climb rate of 1.89m/s and $b = 2.56$m at sea level.

4.3.3 Prototypes Preliminary Configuration

At Aero@UBI, we believe it is possible to reach the podium with a low budget, by the implementation of innovative and audacious concepts. In this 10th ACC edition, the team wants to make use of a pusher configuration by the following reasons:

- A greater extent of laminar flow is achieved in the fuselage, since it nose is not affected by the prop-wash swirled disturbed by turbulent propeller blades wakes.

- The propwash would also increase the drag of the fuselage by the addition of an induced velocity component to the freestream airspeed.

- The lower speeds caused by the fuselage wake increase the total thrust force that the propeller+motor system provides. This concept of wake ingestion propulsion [4] is what the team considers to be the greatest benefit in using a pusher aircraft configuration. Observing the thrust vs airspeed curve in Figure 4, one can see that if the propeller is working in a lower airspeed environment, the thrust increases. This will be most noticeable when the aircraft is flying at its maximum airspeed in the flight competition. Note that this maximum airspeed in the flight competition will be achieved at a rate of descent of about 0.6m/s. In this condition the thrust of the propeller can be extremely low. Thus, a slight difference in the airspeed of the propeller can mean a significant difference in the propeller thrust.

The main initial full scale prototype was then designed in CAD, using openVSP (Figures 23 and 24). The reason behind the design of the rest of the components, and the decisions made after experimentally testing them, are as follows. A secondary initial full scale prototype was also built in order to compare the performances between a pusher and tractor configuration, presented in Figure 26.

- **Wing**: The initial wing consisted in 7 panels, with the aim of approximating its lift distribution with that of an elipse. Theoretically, the predicted results were satisfactory. However, when flight tested despite some initial wing washout torsion, it presented a serious problem regarding wing tip stall. We even had a crash where we needed to spend around 6 months rebuilding the aircraft. An increased wing washout torsion needed to be applied, and it decreased the aircraft performance, as shown in Figure 34 for cruise flight condition ($C_L = 0.25$) and 35 for climb flight condition, by the curves in red. The decrease in C_L/C_D by the implementation of the extra torsion in the eliptical lift distribution wing is 2.97% in cruise speed, and 1.76% at climb speed. In order to solve the wing tip stall issue, a rectangular wing, with a trapezoidal tip was studied (black solid curve). Its C_L/C_D at cruise speed is 8.18% better than the corrected wing of the initial main prototype represented by the red dashed curve, and at climb speed is 2.72% better. When a linear torsion distribution (0°at root, -2°at tip of rectangular panel and -5°at the wingtip) is implemented, the increase comes up to 9.42% at cruise speed and 3.26% at climb (black dashed line versus red dashed line). So, this is the final geometry to be used in the competing aircraft (see Section 10).

- **Tail:** The V-tail configuration was adopted for the main initial full scale prototype (see Figure 22). Studies regarding latero-directional stability were not performed. So, despite a "normal" tail volume coefficient, so the vertical volume coefficient, $\bar{V}_v$, it was not enough to provide adequate latero-directional stability. This was thought to be due to the unconventionally low tail arm length with the exagerated $66°$ rhombus semi-angle. So, in order to correct the issue, the angle between each side of the stabilizer needed to be reduced, which would increase the interference drag between the two tail surfaces, thus invalidating the concept. For the experimental tests, tries to increase the stabilizer span were performed, without satisfactory success. For convenient test flight data acquisition, a T-tail was introduced into the main initial prototype (Figure 22). For the final aircraft, considering that the rhombus semi-angle was decreased to $58.6°$, providing a more generous vertical tail arm, an inverted V-tail is thought to be the ideal solution due to the increase in the horizontal tail volume coefficient, $\bar{V}_h$, for a given tail surface size again the angle between each tail side.

- **Landing Gear:** A single large wheel main landing gear is adopted for two different reasons. The usage of a single wheel reduced the total drag due to lower wet and front areas. Using a conventional

main landing gear, opens a window for misalignment of the two wheels, what greatly increasing the resistance to the movement. The choice for a thick and more elastic wheel is the lawn runway surface. A thin wheel would probably bury itself in the grass. This is observed in full scale sailplanes, where a single large main wheel is mostly used.

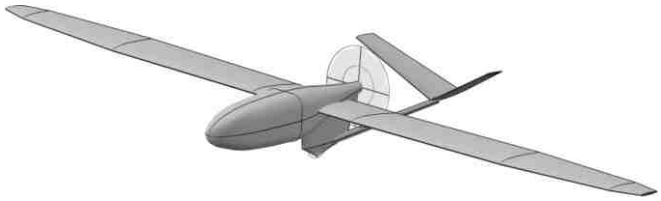

Figure 23: Preliminary design of the main initial full scale prototype with single tail boom configuration.

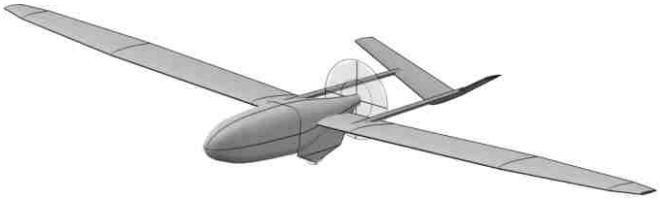

Figure 24: Preliminary design of the main initial full scale prototype with double tail boom configuration.

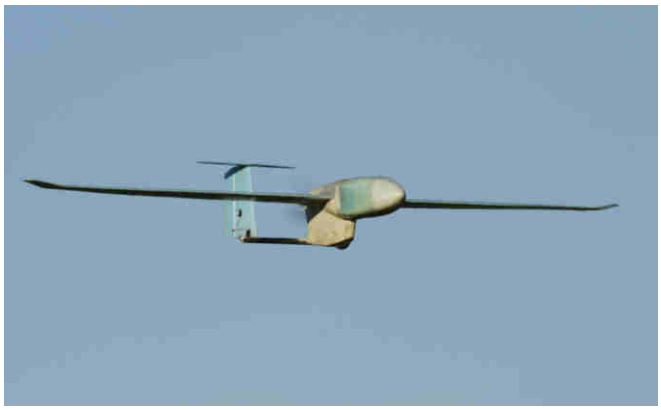

Figure 25: Main initial full scale prototype built and flight tested with the corrected T-tail in order to validate the preliminary design.

Figure 26: Tractor concept aircraft manufactured in order to validate the pusher concept.

In the flight tests with the prototype presented in Figure 25, a maximum cruise airspeed of 27 m/s was registered, and a climb rate of 1.72 m/s with a take-off weight of 41N. Although the results did not perfectly matched what is needed to achieve maximum score at the climb flight, the team believes it was due to the aircraft surface being too "dirty".

4.3.4 Airfoil Design

The design of the airfoil, in terms of performance, is as important to be optimized as the propulsion system alone. Due to this, the team dedicated a lot of time to try to obtain with XFOIL (through XFLR5) the best possible airfoil considering various performance parameters, including aerodynamic at the relevant lift coefficients of maximum cruise airspeed and best climb lift coefficient, transition position and airfoil maximum thickness. Using the original S9000 as the starting point, more than 150 airfoils were created.

Due to the choice of the airfoil having a significant impact on the entire performance of the aircraft, the airfoil must present some key characteristics considered to be a must. With this, the team considered that the airfoil should have a minimum thickness-to-chord ratio close to 9% and it must have low drag coefficient ($C_{d_{min}}$). The iterations were meant to delay the overall transition for any lift coefficient and to increase the aerodynamic efficiency (C_l/C_d) for the cruise and climb conditions, in other words, for C_l=0.263 @ 27 m/s and C_l=0.748 @ 16m/s. This conditions were selected because they are considered the most important phases of the flight task.

Figures 27 to 33 show the difference between the original S9000 airfoil and the final airfoil obtained with the iterations, HS 9000 4X. For sustained level flight with $Re\sqrt{(C_l)} = 150000$, Figures 28 to 33 show the drag polar, lift curve, upper surface transition curve, pitching moment coefficient and aerodynamic efficiency graphs. The geometries of both airfoils are presented in Figure 27.

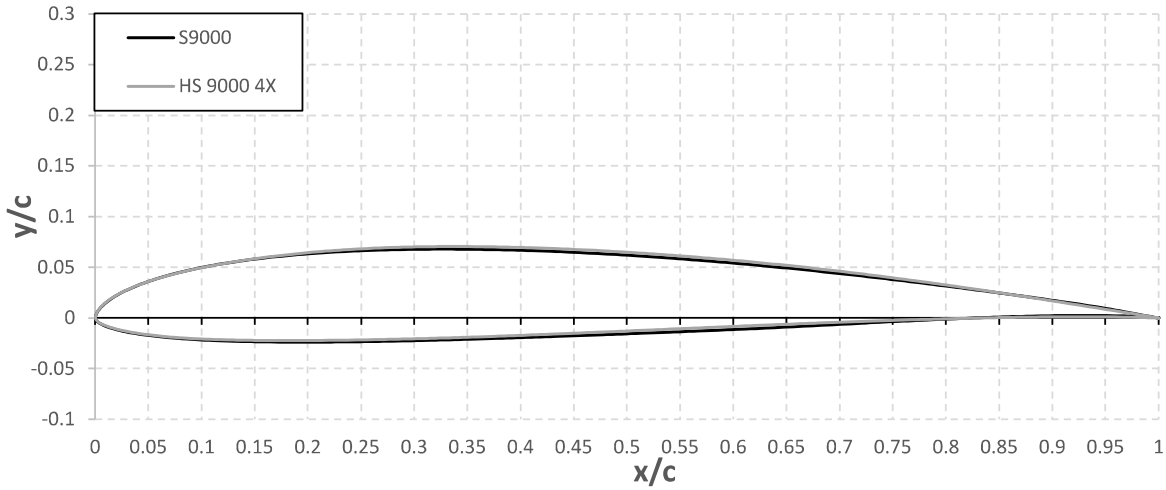

Figure 27: S9000 and HS 9000 4X airfoils.

The geometric characteristics of the HS 9000 4X are a maximum thickness-to-chord ratio of 9.04% at 0.297c and a maximum camber of 2.63% at 0.435c. Comparing the two airfoils, there was an increase of 7.94% of the airfoil aerodynamic efficiency in cruise and 3.70% in the climb flight, allowing the aircraft not only to fly faster but also to fly with more weight.

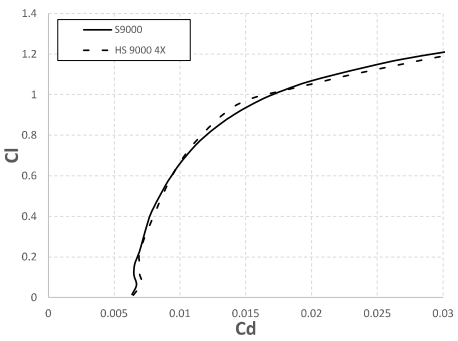

Figure 28: Drag Polar

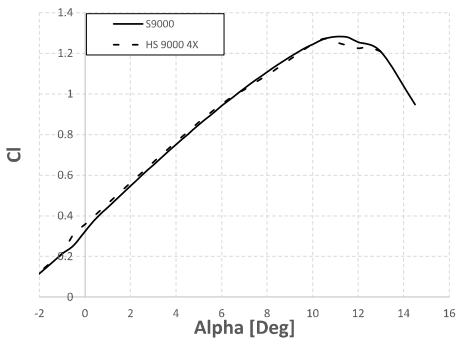

Figure 29: Lift coefficient vs angle of attack

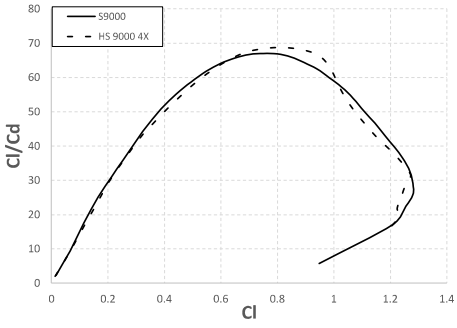

Figure 30: Lift-Drag ratio vs lift coefficient

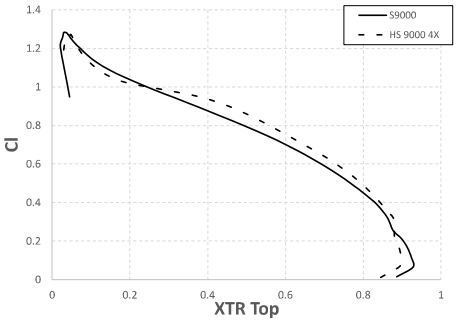

Figure 31: Lift coefficient vs Top transition position

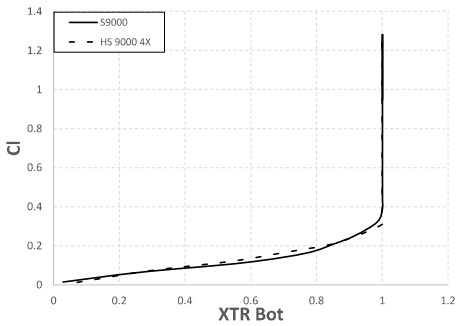

Figure 32: Lift coefficient vs Bottom transition position

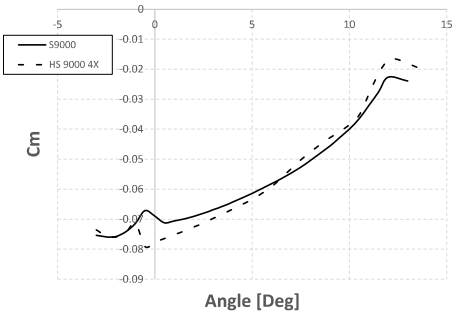

Figure 33: Pitching moment coefficient vs angle of attack

4.4 Flap Selection

With such low cambered airfoil (see Section 4.3.4), the take-off gets critical if the maximum lift coefficient, $C_{l_{max}}$, does not reach a high enough value.. Initially, the team considered using two types of flaps, the Fowler flap and the simple plain flap. Having in mind the tests done in the previous editions of the air cargo challenge, the team promptly realized that the best option was a plain flap because of the added complexity and weight of the Fowler flap, as well as making the pitch trimming more difficult. The initial small scale prototypes also confirmed the effectiveness of a full span flaperon solution. This also allows to use only two servos hidden in the fuselage.

The use of the full span plain flap works as a variable camber flap not only to increase C_{lmax} during the take-off phase by deflecting it down but, also, to decrease the drag coefficient C_d in the cruise phase by deflecting it up. A study was performed in XFLR5 to understand what was the percentage of chord and its deflection so that the aircraft would take-off in the 60 meters. Initially, the team thought it was better to have a higher percentage of chord for the flap section on the root than on the tip. However, the best results were obtained when the flap percentage was 17.5% on both root and tip and for deflections of 20° down for take-off and 1° up for cruise.

4.5 Final Configuration and Wing Size

After all the theoretical (parametric and XFLR5) and experimental work, a final wing configuration was defined. XFLR5 studies showed that a mean aerodynamic chord, c_{mean} of 0.19m would be more suitable. A linear geometric twist of -2°was applied up to the tip of the rectangular wing section, and a geometric twist of -5°was then applied since the end of the geometric section up to the tip of the wing. The final wing geometry can be seen in the Appendices 10. The aircraft is designed to lift-off in 54m, and have a maximum climb rate of 1.89m/s. Vertical tail coefficient is 0.018

4.5.1 Stability and Control

The aircraft was designed to have its CG position close to 25% of the MAC. The tail and the dihedral angle of the wing were sized for the defined values of static margins. The longitudinal static margin chosen was 11%, the directional static margin was 0.051 and the lateral margin was -0.024 in order to ensure both adequate stability and manoeuvrability of the aircraft. These requirements resulted in a horizontal tail volume coefficient of 0.28 and a vertical tail volume coefficient of 0.015.

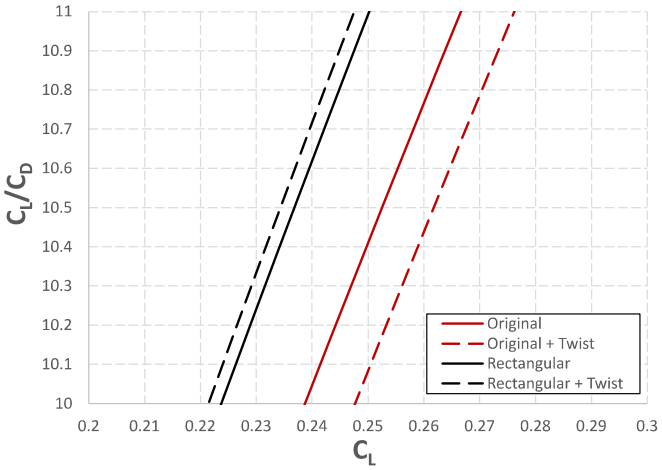

Figure 34: XFLR5 predictions of Lift-to-drag ratio, C_L/C_D versus lift coefficient, C_L at cruise speed, for four airplanes with the same tail but different wing, with pitching moment equal to zero for cruise flight condition.

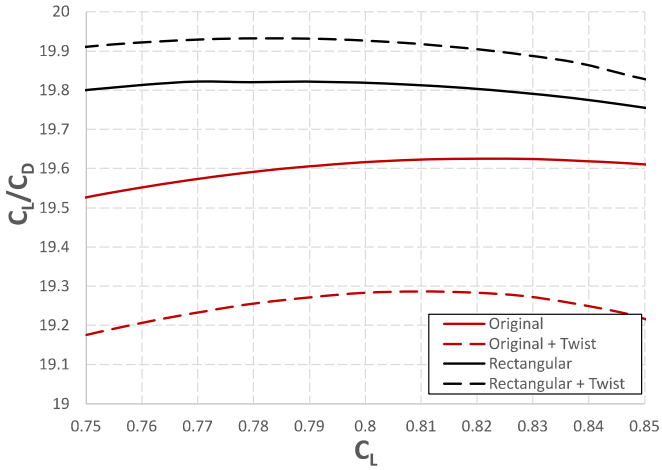

Figure 35: XFLR5 predictions of Lift-to-drag ratio, C_L/C_D versus lift coefficient, C_L at climb speed, for four airplanes with the same tail but different wing, with pitching moment equal to zero for cruise flight condition.

5 Structural Design

The structure was designed to be structurally stable when flying with the maximum predicted payload weight multiplied by the maximum load factor, and during the mandatory ground structural test, when the aircraft is supported by its wing tips.

5.1 Research

In an effort to maximize the payload score, a comparative study of different types of wing structures was performed in order to minimize the wing mass and consequently the empty mass of the aircraft.

5.1.1 Structure Configurations

To achieve the best compromise between a light wing structure and a good aerodynamic performance, four different configurations were considered. Figure 37 shows a representation of each one.

The configurations can be divided into two groups. Load bearing skin wing where all the skin resists the torsion moment and a sandwich is used as spar. D-box wing that have only the skin forward section to support the torsion moment, ribs to transmits the loads from aft part to the D-Box and a C shaped spar. For each configuration a skin made of a sandwich or a skin with a laminate over a core of foam was considered.

Independently from the configuration, the bidirectional CFRP skin and spar webs were sized for shear and torsion loads while the unidirectional CFRP spar caps were sized for bending loads. The critical loads for the wing structure sizing were determined from high load factor in flight,$n = 3$, from heavy hard landing and from ground loading test conditions. For flight conditions that may occur that exceed those considered and possible material defects a safety factor of 1.5 is implemented.

The bending moment, M_x, shear force, Q_y and torsion moment T were calculated at the root for each wing panel.

For the flight case, the following equations were used,

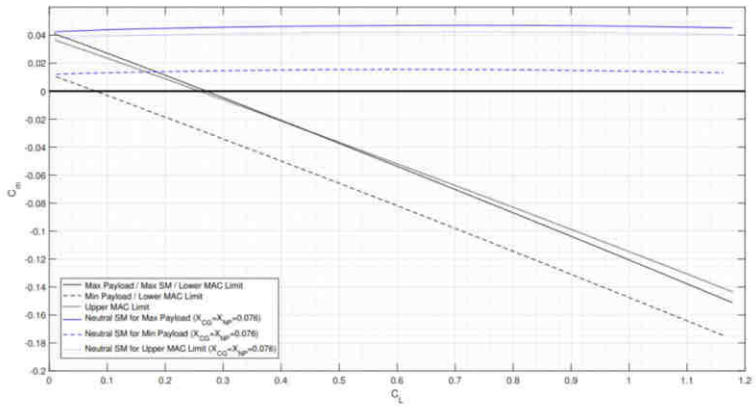

Figure 36: Pitching Moment Coefficient (C_m) as a function of the Lift Coefficient (C_L) for each payload cruise configuration as previously presented in the preliminary report. Results obtained with XFLR5.

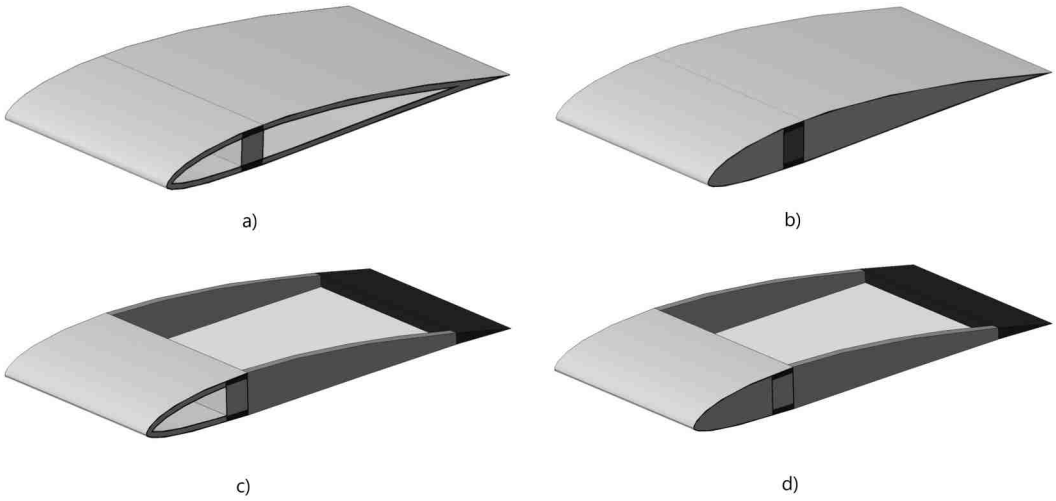

Figure 37: Different configurations of wing structure. a) Load-bearing skin wing sandwich skin; b) Load-bearing skin wing with foam core; c) D-Box sandwich skin; d) D-Box wing with foam.

$$\begin{cases} M_x = \frac{W_y}{2}(\frac{b}{2} - y)^2 \\ Q_y = w_y(\frac{b}{2} - y) \\ T = \frac{1}{2}\rho V^2 C_m c^2(\frac{b}{2} - y) + \frac{1}{2}L_{tb}F_{zt},\ for\ y < 0.18m \\ T = \frac{1}{2}\rho V^2 C_m c^2(\frac{b}{2} - y),\ for\ y \geq 0.18m \end{cases} \tag{14}$$

where $w_y = \frac{nW}{b}$ represents the assumed uniform lift distribution across the span, C_m is the airfoil pitching moment coefficient, L_{tb} is the tail boom length and F_{zt} is the tail force necessary to balance the aircraft.

For the ground analysis, the force and moments were computed through the equations:

$$\begin{cases} M_x = \frac{W}{2}(\frac{b}{2} - y) \\ Q_y = \frac{W}{2} \\ T = \frac{W}{2}(x_{c/4} - x_{winglet-tip}) \end{cases} \tag{15}$$

where $x_{c/4}$ is the longitudinal (chordwise) position of the quarter chord line and $x_{winglet-tip}$ is the winglet leading edge longitudinal position where the aircraft will be held in the ground test.

5.1.2 Construction Techniques

Constructive tests were made during the conceptual design to have a better prediction of the aircraft mass and to improve the method used to build the aircraft.

For the construction of the wing and other components in composite materials, a mold production technique was developed using 3D FDM printing plugs and burlap reinforce plaster molds. The objective of this technique is to decrease the cost and ecological footprint of the molds production and disposal. The technique was improved during the tests that were made to study the different structure configurations.

To make the plaster molds, a wing panel plug is 3D FDM printed and finished to correct the printing defects. Then a dividing surface is created at the leading edge and at the trailing edge to separate both sides of the mold. The first part of the mold is created by placing plaster on the wing plug and on the dividing surface. The second part of the mold is created repeating the process on the other side of the plug and dividing surface.

Figure 38 shows one of the 3D printed wing panel plugs used in the constructive tests is shown and Figure 39 shows the mold made from the same plug.

Figure 38: 3D printed wing panel plug for constructive tests

Figure 39: Burlap reinforced plaster mold for constructive tests

5.1.3 Construction Test and Materials

To carry out the constructive tests and design the structure of the aircraft for the competition, the team made use of the materials that we already had at the university in order to avoid the purchase of additional material.

Regarding the use of composite materials we had available 200g/m^2 woven carbon fiber, 80g/m^2 bidirectional carbon fiber, various unidirectional carbon fibers 50g/m^2 woven glass fiber and 25g/m^2 woven glass fiber. All the fabrics are used along with R&G Epoxy resin L and GL hardeners.

For the manufacturing of sandwich-structured composite cores the team has 1mm and 2mm balsa wood available, and AIREX® foam (60kg/m^3) with 6mm of thickness and EPS foam sheets (30kg/m^3) with any desired thickness. In the full foam core wing configurations considered, the used foam is a 2 component polyurethane foam (35kg/m^3).

Connections and interfaces between various components of the aircraft are made with plywood and 3D printing components.

Although the polyurethane foam has a tabulated density of 35kg/m^3, we did some tests to find out what the density would be under the conditions it would be used because it affected the foam expansion. The result was around 38kg/m^3, slightly above the specified density. In addition to these tests, we also glued two foam blocks to simulate the closing of the molds with full foam core configurations as this junction would not let the used foam to fully expand, increasing the density of the final product. For the interface of the two blocks 2 component polyurethane foam and spray polyurethane foam (SPF) were used. The result was a mass increment due to the interface similar both both solution of around 0.42kg/m^2. Table 6 summarizes the tests data.

Specimen ID	Connection foam	Dimension [mm^3]	Mass [g]	Mass increment [kg/m^2]
1	Without connection (Control)	73×44×21	2.6	-
2	Polytherane (Spray)	79×50×13	3.7	0.436
3	Polytherane (Spray)	78×50×13	3.6	0.422
4	Polytherane (2 component)	78×50×14	3.6	0.422
5	Polytherane (2 component)	81×39×15	3.1	0.396

Table 6: Tests of polyurethane core foam interface weight.

5.1.4 Structure configuration Mass

Table 7 shows the calculated mass for each configuration. A skin ±45° orientation layers was considered with of 80 g/m^2 CFRP and a 1mm balsa wood core for the skin sandwich. The spar, in all cases, is a sandwich with a 6mm thick 60 kg/m^3 AIREX® foam and a web of CFRP equal to the skin. The spar caps are unidirectional CFRP aligned with the wing span. For the foam core configuration 30 kg/m3 EPS foam cores were used, with a mass increment of 0.08kg/m^2 on the bonding surfaces to account for the resin needed to glue the surfaces. In these calculations, only the wing rectangular section was considered.

Configuration	Mass [kg]
Load-Bearing skin wing sandwich skin	0.714
Load-Bearing skin wing foam core	0.502
D-box wing sandwich skin	0.330
D-box wing foam core	0.289

Table 7: Mass prediction for the four configurations

From the gathered data we concluded that, for the available material, by using the D-box Wing configuration, a considerable wing mass can be save. Additionally, the use of a full foam core for small chords sizes can reduce the mass of the wing.

With these conclusions, two wing sections panels were built to validate the calculations and compare two D-box configurations: one that uses balsa wood ribs with heat shrink film covering and another that has a full foam core in the airfoil backwards covered with a single 25g/m^2 GFRP layer. Figures 40 and 41 show the finished wing panels.

Table 8 summarizes the results obtained from the wing panels constructive tests and compares those with the respected estimated mass. The experimental mass, $m_{Experimental}$ was measured and compared

Figure 40: D-Box wing section with balsa wood ribs and heat shrink film covering

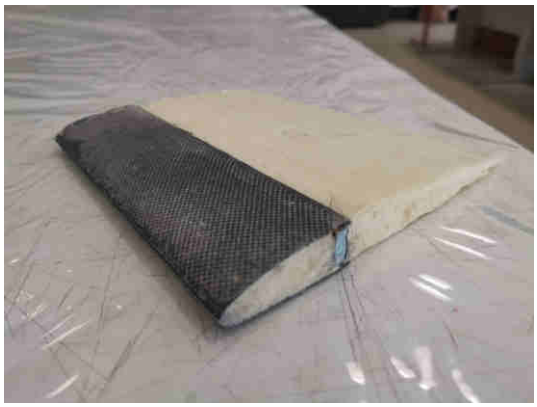

Figure 41: D-Box wing section with full foam core and a thin GFRP layer

to the expected calculated mass for the wing panel, $m_{Expected}$. The relative difference, m_{RD}, between the expected and the experimental value, is computed with Equation (16).

$$m_{RD} = \frac{m_{Experimental} - m_{Expected}}{m_{Experimental}} \tag{16}$$

	$m_{Experimental}$ [g]	$m_{Expected}$ [g]	m_{RD} [%]
D-box full foam core	58.4	55.1	5.4
D-box with balsa ribs and film	35.3	29.9	15.3

Table 8: Results of constructive tests

5.2 Wing

The final wing structure consists of a CFRP D-box wing with a full foam core and C-shape spar. While the D-box with balsa ribs and film configuration was proven to be lighter, it also added higher complexity to the manufacturing process, the design of the flaperon hinge would add a rear spar mass that was not accounted for and the aerodynamic performance would be affected as the film does not comply with the airfoil geometry.

In order to allow the disassembling of the wings to the transporting box, it is divided in three panels, one central panel and two tip panels. The D-box wing structure concept is based on a CFRP laminate over a Polyurethane foam. The laminate skin uses a ±45° orientation layer of 200 g/m² CFRP for the central panel and ±45° orientation layer of 80 g/m² CFRP. The main spar is also made of a sandwich but in this case the core is a 6mm thick 60 kg/m³ AIREX® foam. The spar caps are placed at the maximum thickness position of the aerofoil. For the spar caps unidirectional CFRP aligned with the wing span is used.

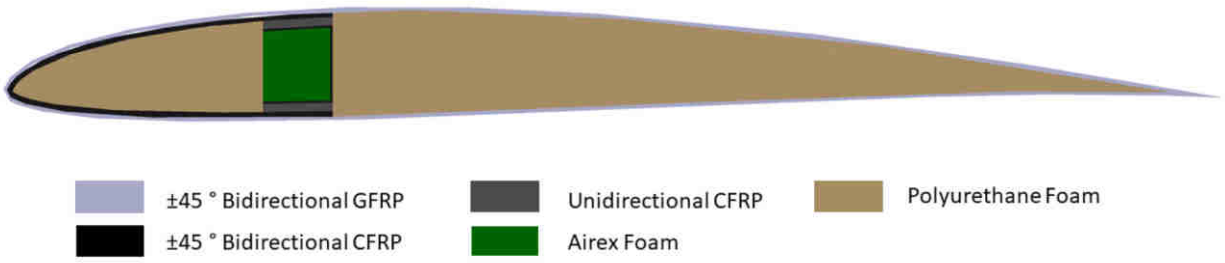

Figure 42: Wing structure configuration

5.3 Fuselage

The fuselage skin is made of a thick carbon fibre reinforced polymer (CRFP) laminate. The laminate consists of two ±45° orientation layers of 200 g/m² CFRP. The skin is reinforced with a plywood frame at the positions where it is joined to the wing and the motor.

To facilitate the loading process of the payload the fuselage is divided into two modules seen in the technical drawings. The front module contains most of the payload bags and the back module contains the systems.

The wing-fuselage connection is made between the wing central panel and the back module of the fuselage, meaning that the wing is built-in to back module.

The main landing gear consists of a single wheel incorporated in the front module of the fuselage. The main wheel is connected to a plywood box.

5.4 Tail

The tail structure must support both trim and manoeuvring loads when flying. Equation (17) gives the equilibrium loads necessary to balance the wing pitching moment and the lift moment created from the distance of the center of gravity to aerodynamic center.

$$F_{zt} = -\frac{0.5\rho S c C_m}{l_T - x_w} V^2 - nW \frac{x_w}{l_T - x_w} \tag{17}$$

The manoeuvring loads were determined for three distinct fight conditions at the manoeuvring airspeed: a zero sideslip angle with the rudder control in maximum deflection, a high angle of attack with the rudder control in maximum deflection and a high angle of attack with the rudder control in neutral position.

The sum of both types of loads represents around 18% the load of the wing. Therefore tail surfaces will be built with EPS conventional ribs with 1mm thick balsa wood caps and heat shrink film covering spars a 2mm caps with EPS foam web sandwich tapered main and rear spars are used. The ruddervators control surfaces use a similar structure. The leading edge is made of solid EPS foam core and 1mm front skin.

5.5 Tail Booms

The tail booms are used to connect the inverted-V tail surfaces to the wings and also contain the secondary landing gear (see appendix "Drawings"). The tail booms, cheap GFRP fishing rod tapered tubes are used to support the tail loads during flight with minimal deflection and also the landing loads from the secondary landing gear.

Due to limited space in the transportation box, the tail booms must provide easy assembly and disassembly of the wings. For that, the use of a frontal end support tube that fits in the tail boom front section and is fixed to the torsion box of the wing is considered.A foam fairing is used to reduce the interference drag between the wing lower surface and the tail boom.

At the end of each tail boom there is a small wheel which work as a part of the secondary landing gear.

6 Systems

The team's choice of systems was limited by the regulations as exposed in Section 4.4 of the Regulations Handbook.

The systems installed onboard the aircraft are as follows: Motor & Propeller; Motor Battery; Electronic Speed Controller (ESC); Radio Control Receiver; Servos; Data Acquisition System.

Rule **4.4.7** is being followed, since there is no way to modify the aircraft's geometry or move the control surfaces automatically, with the systems described above.

6.1 RX battery & BEC

The battery chosen for this task is the LiPo-Akku TopFuel 500 ECO-RX. Package which is in conformity with **4.4.6**. To make sure the voltage in the receiver remains at 5 V during the whole flight, a battery elimination circuit (BEC) connects the RX battery to the receiver. The chosen BEC will be the KINGKONG 5 V 3 A Switching Power UBEC.

6.2 Receiver and Radio Control

The operating frequency of our radio system will be 2.4 GHz, an allowed frequency in Germany, as per rule **4.4.6**. The radio is a Futaba 14SG and the receiver is a R7008SB.

6.3 Servos

The team has decided there will be only one type of servo used in the aircraft: Corona939MG Digital Metal Gear Servo. This servo should be able to withstand the aerodynamic forces in the control surfaces as required in **4.4.6**. However, since the aircraft has not been built, at this point there cannot be full certainty about the servos choice and further tests need to be made.

6.4 Data Acquisition System

The data acquisition system will be the one provided by the organizing committee. It uses a Unilog GPS Logger 3 to get the altitude and GPS Data. This logger is approved and tested by several model aircraft competitions.

7 Payload Prediction

The aerodynamics and propulsion calculations allowed to obtain Equation (18) predicting the payload in function of the air density.

$$m_{Pay}[kg] = 2.468\rho_{air}[kg/m^3] + 0.4235 \tag{18}$$

8 Center of Gravity

The center of gravity of the aircraft was computed considering the constructive test results and the predictions of the aircraft components' masses. The datum line was positioned at the rhombus center and the positive x-axis direction points towards the tail. Table 9 presents the CG position for the full loaded aircraft case.

N°	Components	Weight	Quantity	Total weight	dx_{cg}	W^*dx_{cg}
1	Wing central panel	250	1	250	80	20000
2	Wing tips	150	2	300	82	24600
3	V-tail	50	1	50	730	36500
4	Cargo Bay	250	1	270	35	9450
5	Internal structure	35	1	35	80	2720
6	Tail Boom	75	2	170	352	52800
7	Landing Gear	50	1	50	18	900
8	Motor	181	1	181	410	74210
9	Propeller	10	1	10	440	4400
10	Motor battery	268	1	268	270	72360
11	ESC	12	1	12	360	4320
12	BEC	12	1	12	320	3840
13	Receiver	10	1	10	330	3300
14	Servo V-tail	9	2	18	740	13320
15	Servo wing	9	4	36	100	3600
16	Measuring equipment	150	1	150	215	32250
17	Velcro and adhesives	12	1	12	320	3840
18	Payload	300	11	3300	-3	-99000
	Structure Weight	1116			**x_{cg}**	51.518
	Systems Weight	697			**%mac**	0.251
	Total Empty Weight	1813				
	Take-off Weight	5114				

Table 9: Masses and location of each component of the aircraft corresponding to Munich altitude, 520 m.

The decrease of mass of the first bag from the full payload is also critical because there isn't must room to adjust the bags position so it was also tested to seen if the variation stay in the static margin considered. After removing the first bag the empty space left will be enough to adjust the CG position. However was calculated a minimum of four bags at the nose of the fuselage to make it possible for take-off.

9 Outlook

At the moment we are completely focus on the moulds and aircraft manufacturing process. We are starting the moulds design and construction base on the previous tests made for wing tests sections. We are also completing the manufacturing preparation of aircraft parts that don't require moulds to produce that will be build in parallel with the Cargo bay and wing mould.

Deadlines for the manufacturing process has been defined in order to finish the aircraft in time for presenting the flight proof:

10/5 - Start cargo bay and wing mould's construction;

15/5 - Start stabilisers' construction;

25/5 - Start cargo bay's and wing's construction;

20/7 - Deadline for proof flight video.

10 Drawings

The four technical drawings required by the regulations are presented at the end of the document.

References

[1] Garcia G.L. and Gamboa P.V. "Mass prediticton models for air cargo challenge aircraft". In: *The Aeronautical Journal* (2021).

[2] Douglas F. Hunsaker and Warren Phillips. "Ludwig Prandtl's 1933 Paper Concerning Wings for Minimum Induced Drag, Translation and Commentary". In: *AIAA Scitech 2020 Forum*. DOI: 10.2514/6.2020-0644.

[3] Edson Lopes Barbosa Leite. *Estudo do Confinamento da Hélice para o Sistema Propulsivo do Avião do Air Cargo Challenge 2021/2022*. Jan. 2022.

[4] Leroy H. Smith. "Wake ingestion propulsion benefit". In: *Journal of Propulsion and Power* 9.1 (1993), pp. 74–82. DOI: 10.2514/3.11487.

[5] Viktor Zombori. *Study of Electronic Speed Control Strategies for a Fixed Battery, Motor and Propeller Aircraft Propulsion Set*. Sept. 2021.

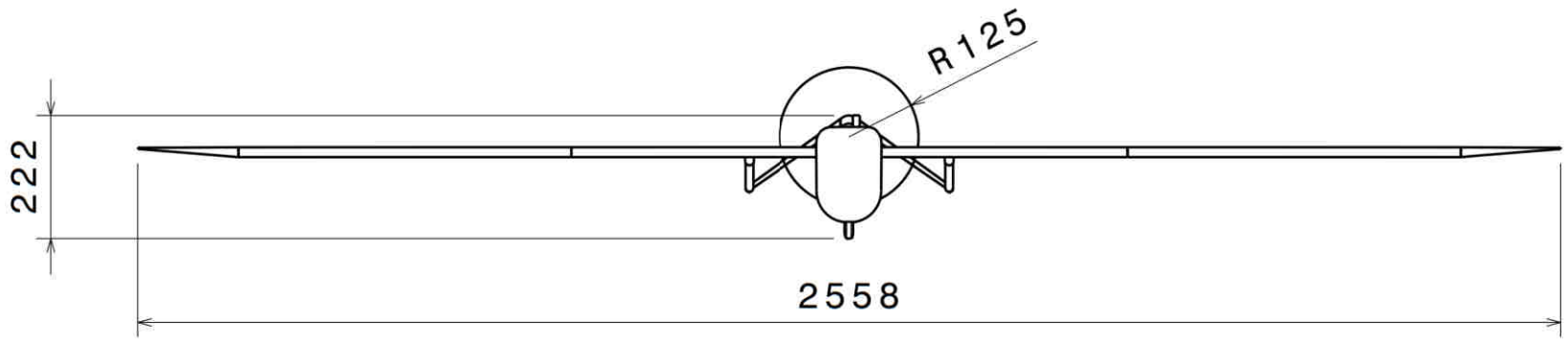

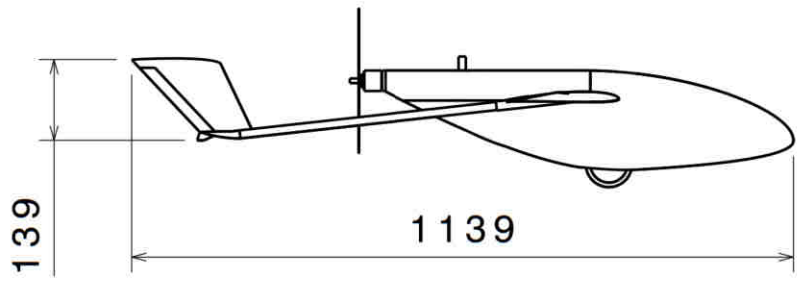

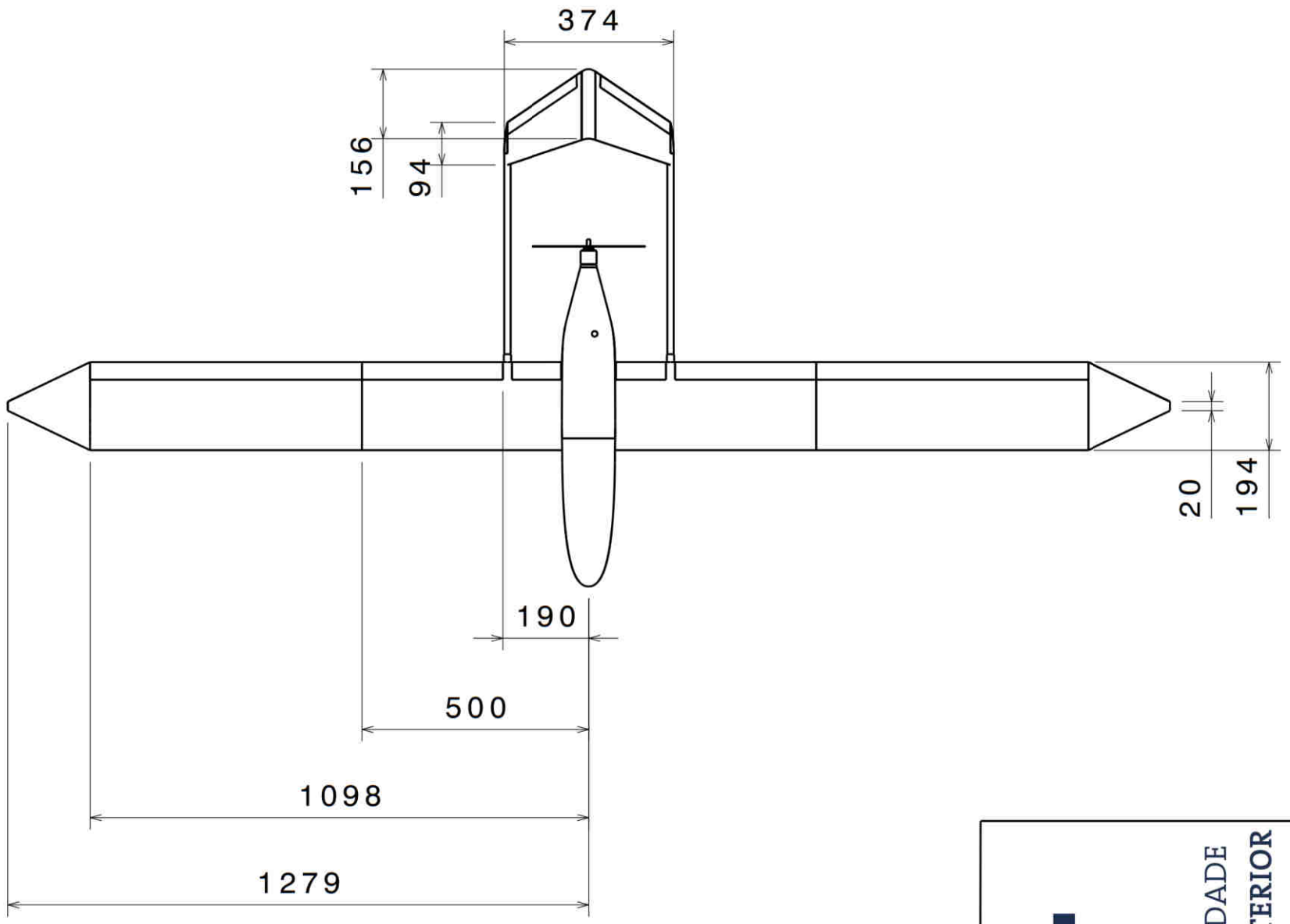

Element	Projected area[m^2]
Wing	0.4661
V-Tail (Vertical)	0.0317
V-Tail (Horizontal)	0.0449
Airfoil	HS 9000 4X
	Volume [m^3]
Fuselage	0.0081

UNIVERSIDADE BEIRA INTERIOR

Aero@UBI

3 - view drawing

Date 30/04/2022 | Scale 1:13 | Size A3 | Drawing no. 1

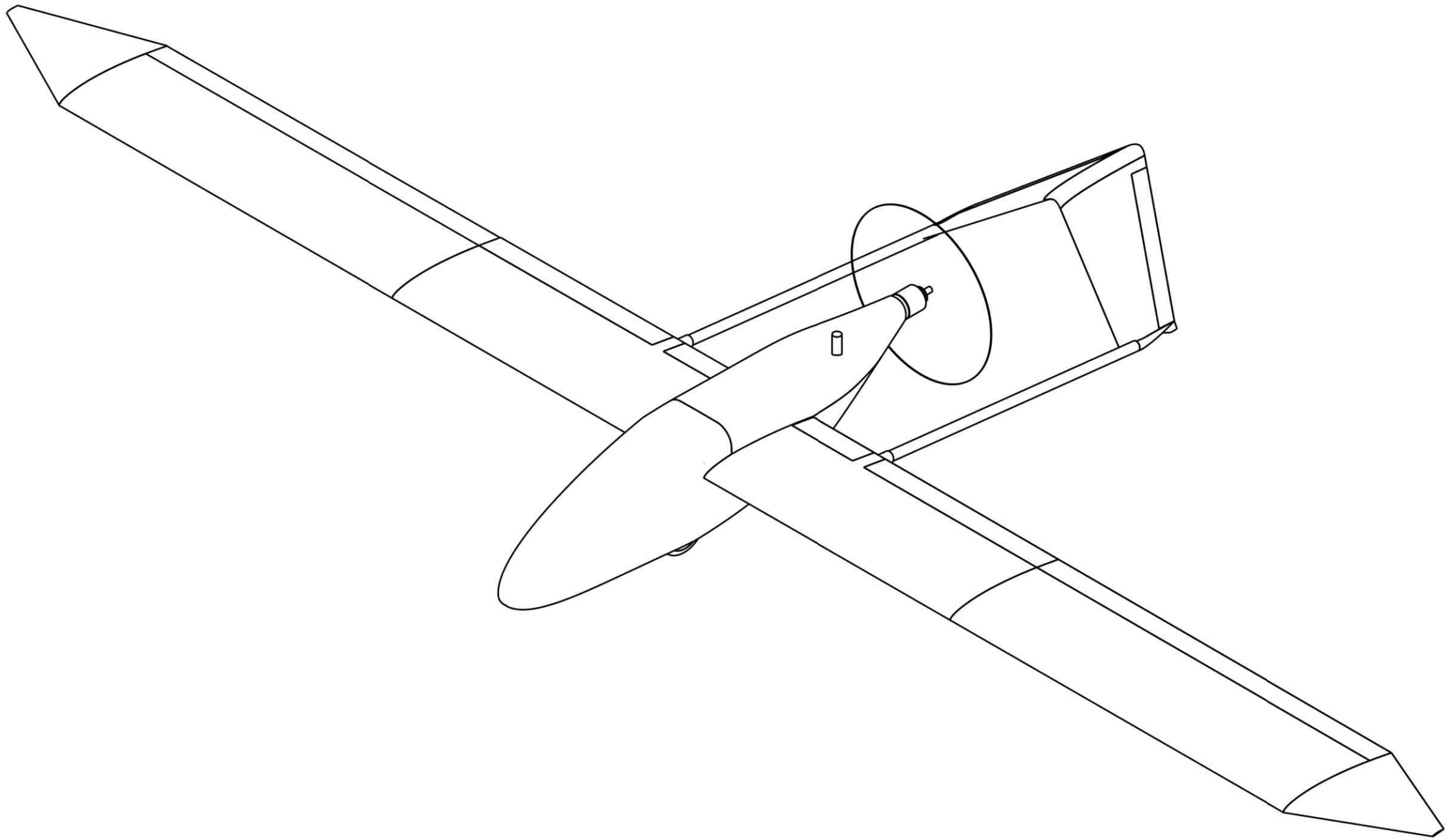

UNIVERSIDADE BEIRA INTERIOR

Aero@UBI

Isometric view

AERO@UBI

Date 30/04/2022	Scale 1:6	Size A3	Drawing no. 2

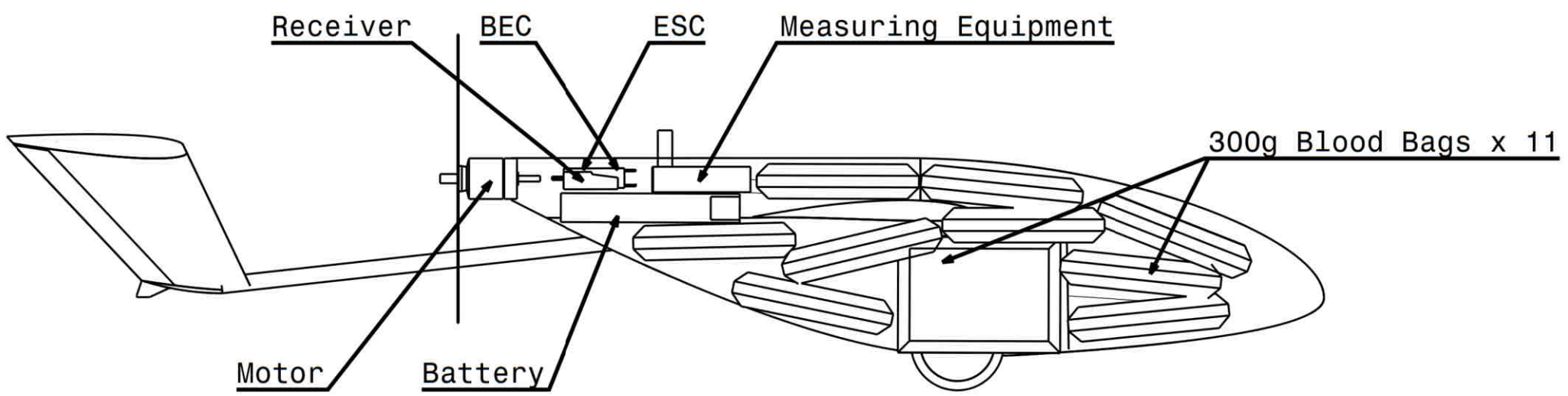

Scale: 1:5

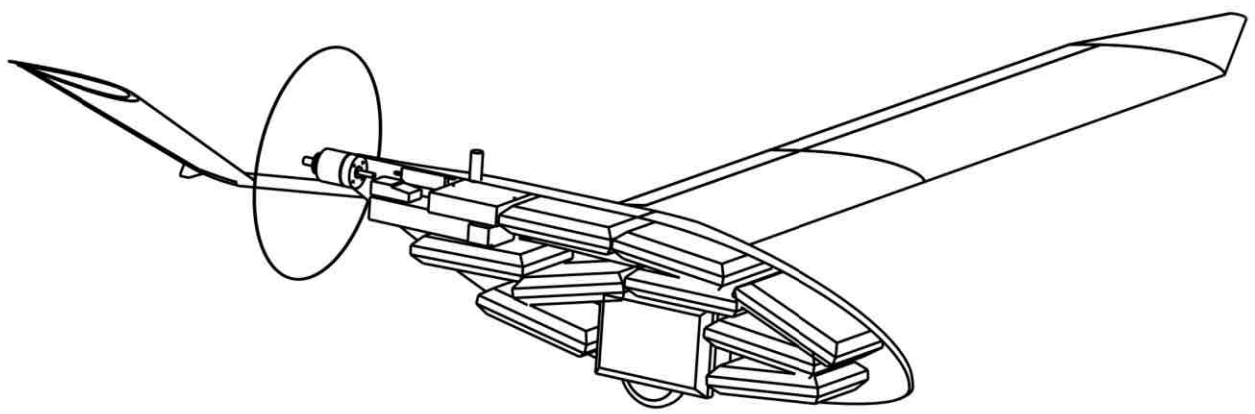

Scale: 1:8

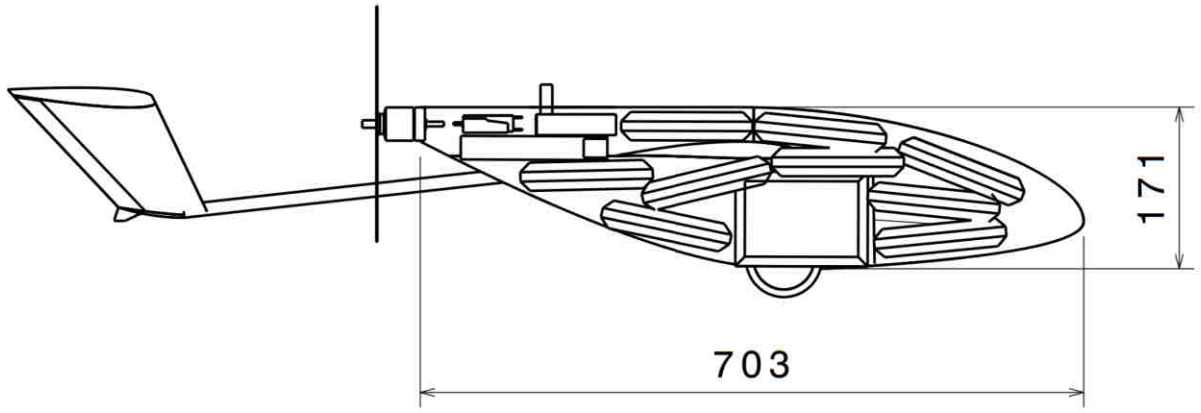

Scale: 1:8

UNIVERSIDADE BEIRA INTERIOR

Aero@UBI

Cargo bay,
RC receiver position,
Measuring equipment

Date 30/04/2022	Scale Variable	Size A3	Drawing no. 3

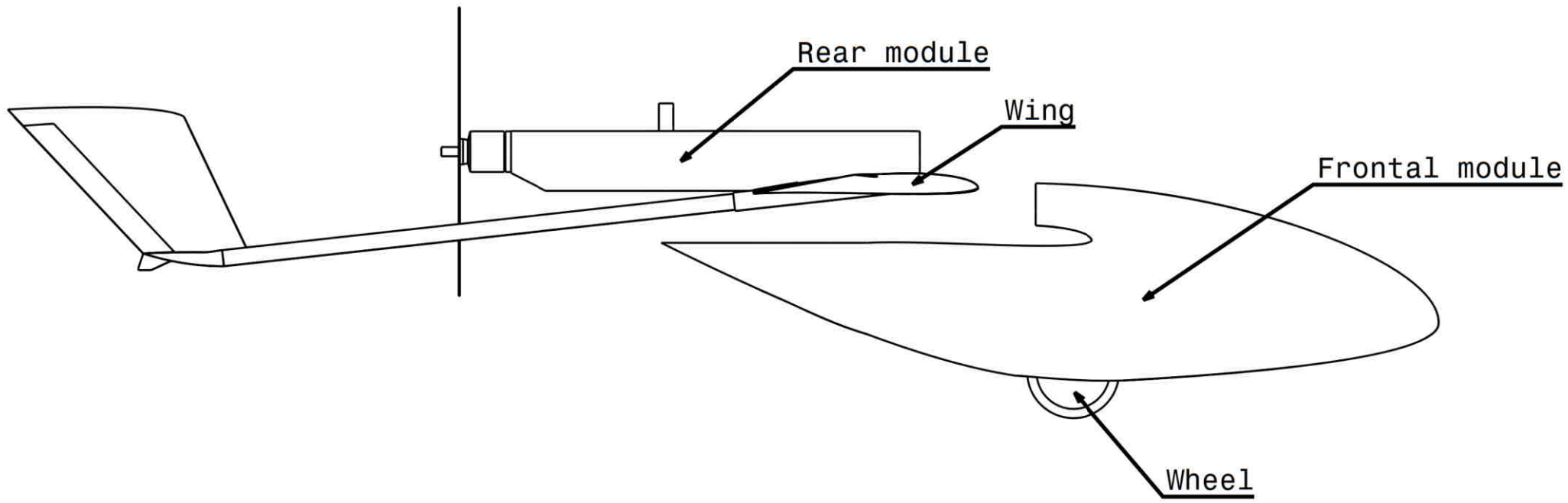

Scale: 1:5

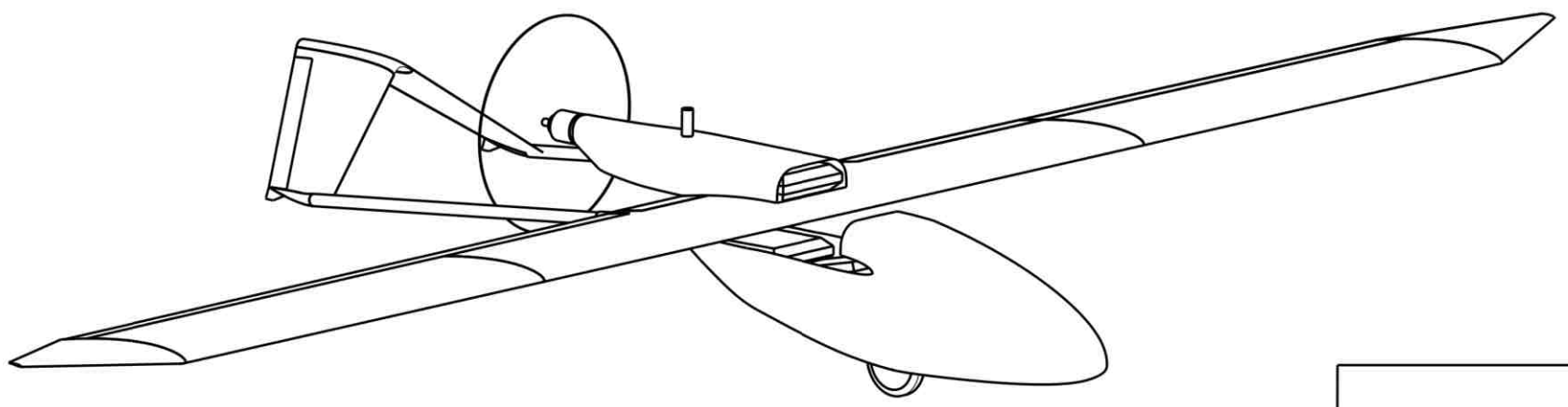

Scale: 1:8

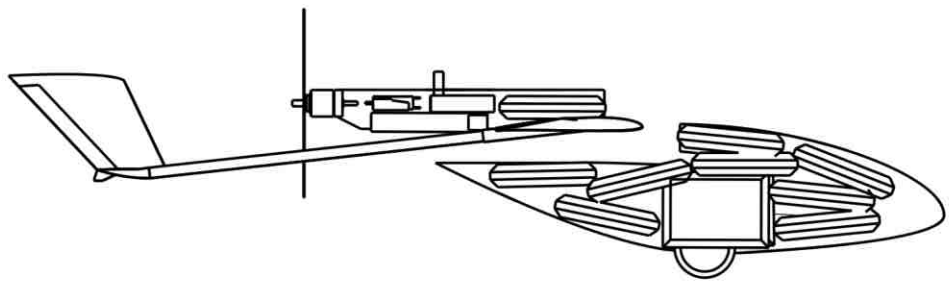

Scale: 1:10

UNIVERSIDADE BEIRA INTERIOR

Aero@UBI

Modular System Implementation

Date 30/04/2022 | Scale Variable | Size A3 | Drawing no. 4